

SMAST Technical Report 16-0402

Assessing Uncertainties in CODAR High Frequency-Derived Surface Current Estimates in the western Gulf of Maine

Shawna L. King and Wendell S. Brown

OCEAN Observation Laboratory (OCEANOL)
School for Marine Science and Technology
University of Massachusetts at Dartmouth
New Bedford, MA

1 Introduction

Between 1994 and 2003 an average of 269 people a year died after the United States Coast Guard (USCG) was notified of an emergency (Schaefer, 2003). Many of these deaths might have been prevented had the USCG been able to find the victims quicker and more efficiently. In search and rescue efforts it is essential that the target is recovered in as short a period of time as possible to increase chance of survival-usually within twenty-four hours (Thompson et al, 2003). Depending on the temperature of the water as well as the safety gear that a person is wearing, hypothermia and exhaustion can set in and even a few minutes can make the difference between recovering a body and bringing someone in alive. The methods traditionally used by the United States Coast Guard to find a target drifting in the ocean has significantly higher levels of uncertainty than those utilizing high frequency radar current estimates, resulting in much larger search areas that require more resources in order to cover fully (O'Donnell et al, 2005).

One of the largest variables that affect the amount of time it takes to find the target is the area that needs to be searched which is a function of the uncertainty in the predicted location. It takes a large amount of time and resources to adequately search an area as it is often difficult to see a target among the waves and retrieve them even in relatively calm weather with low seas; even a small reduction in the area that needs to be searched can greatly reduce the time it takes to recover the target. The size of the search field is determined mainly by the uncertainty in the surface current and simulated surface drifters as a function of time from the last known location (Ullman et al, 2003 and 2006). Quantifying and finding ways to reduce the uncertainty in predicting a target's location is essential to maximize the efficiency and success of search and rescue operations.

Traditional Methods for Search and Rescue: All methods of finding people or any other objects drifting in the ocean start with determining a last known position (LKP) and then estimate a predicted trajectory of the target based on successive surface displacements ($\Delta\mathbf{x}$) over time intervals (Δt). This depends strongly on estimated surface currents \vec{U}_T according to

$$\Delta\mathbf{x}/\Delta t = \vec{U}_T(\mathbf{r}, t) = \Delta\mathbf{r} \quad (1)$$

A drifter trajectory can be constructed from a series of finite displacements ($\Delta\mathbf{r}$) as shown in Figure 1 where an estimate over the time interval $\Delta t = \mathbf{t}_0 - \mathbf{t}$ can be obtained from the finite difference form:

$$\Delta\mathbf{r}/\Delta t = \vec{U}_T(\mathbf{r}, t) \quad (2a)$$

or

$$\Delta \mathbf{r} = \vec{U}_T(\mathbf{r}, t) \Delta t \quad (2b)$$

where \mathbf{r} is the target location at time t . The challenge is to estimate the velocity $\vec{U}_T(\mathbf{r}, t)$ and this is where the different methods come in.

Until earlier this year, the U.S. Coast Guard practice was to use only NOAA tidal current predictions for closest station, and assume spatial uniformity of surface currents to predict the trajectory of a person or object in the water (Ullman et al, 2003). Here the “closest station” refers to the NOAA station nearest the starting location of the drifter. One of the problems with this method is that all of the tide stations are on the coast and are irregularly spaced (Figure 2).

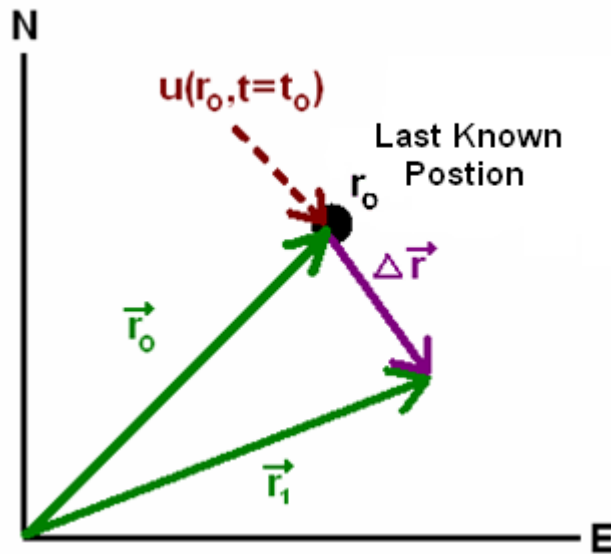


Figure 1. Starting from the last known position (LKP, \mathbf{r}_0) it is possible to estimate the displacement of a particle ($\Delta \mathbf{r}$) from the product of the estimated velocity ($\mathbf{u}(\mathbf{r}_0, t=t_0)$) and the time step (Δt).

Another issue is that the tidal current predictions from the same station are used throughout the simulation even if the drifter passes closer to another station (O'Donnell et al, 2005). This method leads to typical separation differences (i.e. uncertainties) of 10-20km in object position after three hours between the Coast Guard predicted trajectory and that of an actual drifter used in tests. The uncertainty can increase near the coast where topography has a significant effect on currents because NOAA currents are assumed to be spatially homogeneous (Ullman, et al. 2003).

The second traditional method that has been used for search and rescue is the most simplistic albeit theoretically unrealistic method as it does not take into account the constant movement of the ocean, this method assumes that the drifter did not move from its last known position and that $\vec{U}_T(\mathbf{r}, t) = \Delta \mathbf{r} / \Delta t = \mathbf{0}$. It is usually employed in areas where little is known about surface current behavior or where the currents are thought to be minimal. Despite being unrealistic in the idea that an object floating in the ocean will not move over the span of several hours, this

method does show a consistently lower uncertainty than predictions based on NOAA tide data (O'Donnell et al, 2005).



Figure 2. Locations of NOAA tide stations in the western Gulf of Maine. (NOAA CO-OPS, 2007)

New Method for Search and Rescue-Use of High Frequency Radar: Ullman et al. (2006; 2003) have shown that by using high frequency (HF) radar derived current data it is possible to obtain predictions of a floating object's trajectory with uncertainties approximately half that of methods traditionally used by the United States Coast guard. Ullman et al. (2003) emphasized the potential value of HF radar for search and rescue over that of the traditional methods that they had employed.

One method for the use of HF radar to predict the trajectories of “surface drifters” from a last known location, is a short term prediction system (STPS; O’Donnell et al, 2005) and is the method currently in use by the USCG (NOAA, 2009). This method combines surface current observations mostly from land-based HF radar, tidal currents, and meteorological data with an algorithm to predict drifter trajectories. Harmonic analysis is used to isolate the tidal component of the surface current from HF radar surface current estimates as well as current estimates from other sources that have been collected for a month or more. Then the tidal currents may be modeled separately from the non-tidal currents. The main drawback to using STPS is that it requires at least 30 consecutive days of both surface current and meteorology data from several different sources to assimilate to create the algorithm parameters before predictions can be made.

An alternate method for the use of HF radar data as described by Ullman, et al. (2006; 2003), is far simpler in that it incorporates only the HF radar surface current estimates to approximate $\vec{U}_T(\mathbf{r}, t)$. The main drawback to using this method is that there needs to be continuous radar coverage in the area of the target for the time period in question. Here Ullman et al. (2006) use only Coastal Ocean Dynamics Applications Radar (CODAR) derived currents (\mathbf{U}_{radar}) to estimate the true current for a given time step according to

$$\vec{U}_T(\mathbf{r}, t) = \mathbf{U}_{radar} + \delta\mathbf{u} + \mathbf{u}_t = \mathbf{U}_{radar} + \mathbf{u}', \quad (3)$$

where $\delta\mathbf{u}$ is the measurement uncertainty, and \mathbf{u}_t is sub-grid scale variations in velocity. Because of the difficulty separating the measurement uncertainty and uncertainty due to unmeasured small scale variations in velocity, both are combined into a single uncertainty term (\mathbf{u}').

Since four out of five of the Coast Guard's search and rescue cases take place within 100km of the shore, researchers (Ullman et al., 2006 and 2003; O'Donnell et al., 2005) have begun to use CODAR to obtain ocean surface current estimates needed by both the STPS and the CODAR only methods. The following explains the details of the CODAR surface current measurement and thus the possible sources of uncertainty in the use of CODAR to measure surface currents.

CODAR-Related Methods: CODAR is a land based high frequency radar that is used to estimate and map ocean surface currents. The long range CODAR SeaSonde has a range up to 200km from shore. Each station transmits a 4.8 MHz radar signal for 0.5 seconds over typical azimuths of 150°. During the following 0.5 seconds, it receives the returned signal that has been Bragg-backscattered off of surface waves (see Figure 3). Bragg backscattering occurs because of a resonance between the transmitted signal and an ocean wave with a wavelength (or 30m for a 4.8 Mhz signal) which is half that of the transmitted signal. The frequency of the backscattered Bragg signal is Doppler-shifted by the movement of the wave plus any underlying ocean current in the upper couple of meters. The waves, which are typically much speedier than the ocean currents, can be moving toward (away) from the receiver (Figure 3). The associated positive and negative Doppler-shifted frequencies establish the “zero surface current” reference frame as shown in Figure 4. The radial ocean current relative to the Bragg waves is determined from the frequency offset of the two Bragg peaks relative to their zero surface current position (Figure 4).

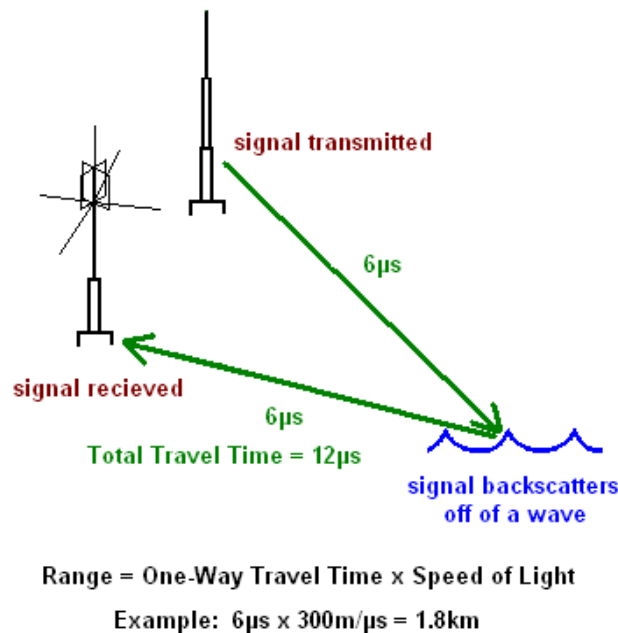


Figure 3. The HF radar signal that is transmitted reflects off of waves moving directly towards or away from the site and is picked up by the receiver. The range of the wave is calculated from the round trip transit time using known speed of the signal.

The backscattered returns are received from an electronic grid of cells or patches of ocean covering the offshore ocean surface (Figure 5). Each individual radial current estimate has a particular range and bearing. The range of the cells along a particular radial is determined by the

time delay in the return of the backscattered signal relative to the transmitted signal (Figures 3 and 5). Although the cell width varies in this cylindrical coordinate system, it is approximately 6km for a 4.8MHz system. For the CODAR HF radar system the bearing of a particular cell is found by feeding the signals from the receiving antenna (a monopole and two loop antennas) into the Multiple Signal Classification algorithm (MUSIC-a proprietary algorithm of CODAR Ocean Sensors). This scheme provides CODAR bearing resolutions of 5 degrees of azimuth. The one second estimates of surface radial current from each cell are very noisy (i.e., highly variable). This one second information is necessary to form current estimates at one or two bearings at a particular range. To reduce the noise, the one second backscattered returns are typically averaged for 3 hours to produce a radial current estimate with an acceptable uncertainty for a particular cell (e.g., 6km x 6km at a range of 69km). All the surface current measurements within each cell (6km range x 5 degree bearing or approximately from the receiver) are averaged to obtain a single vector surface current estimate.

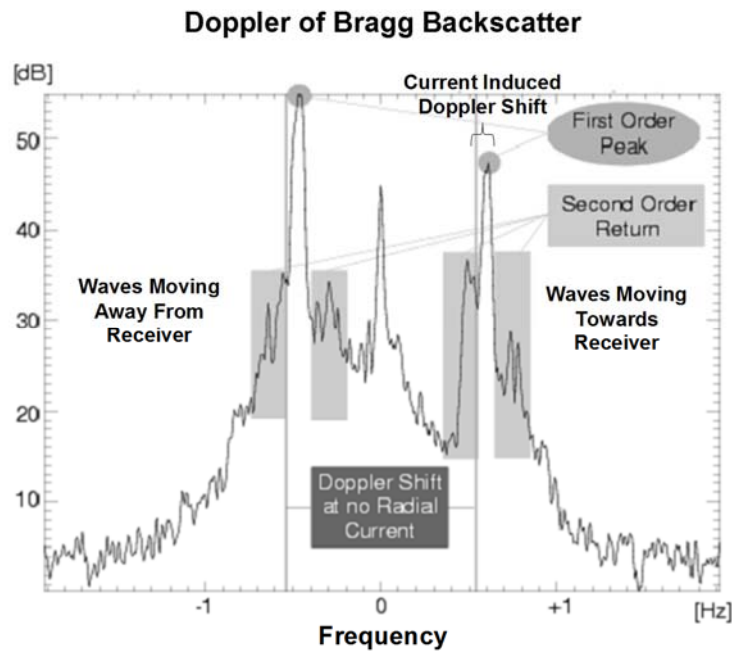


Figure 4. A Doppler spectrum graph of the Bragg signal reflected off waves (a) moving away from the receiver (at frequencies <0) and (b) moving towards from the receiver (frequencies >0). The positive shift of the Doppler peaks relative to their zero current references (solid lines) indicates that the current itself is moving towards the receiver.

While this temporal and spatial averaging results in lower resolution and obscures the small scale current fluctuations, the uncertainty in the individual radial current estimates is reduced to an acceptable level. The current estimates in the cells farthest away from the station are affected the most by the spatial averaging because area of each cell is the larger ($5.8\text{km} \times 5.8\text{km} \times \tan [2.5 \text{ degrees}] = 1.47\text{km}^2$ difference per 5.8km range cell distance) than the cells closer to the station because of the increasing distance between two adjacent radials with the distance away from the station.

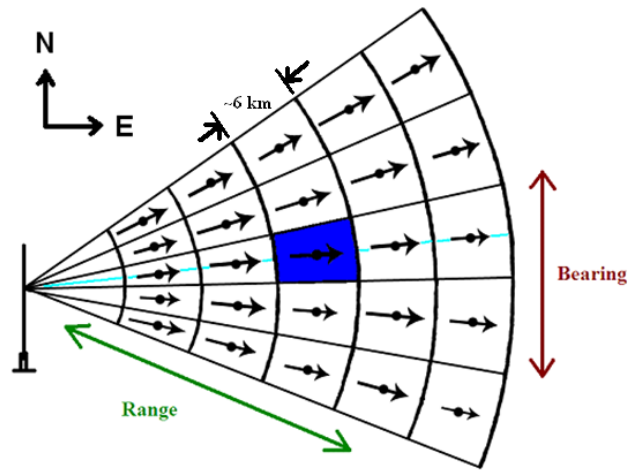


Figure 5. An example of the radial current estimates in the grid of cells from a single 4.8 MHz CODAR station. Each radial current estimate corresponds to a defined range bin (about 6 km out to about 200 km) and bearing bin (5°).

Since a single CODAR station can only obtain current estimates along radials, two or more stations with radial current estimates covering the same region are required in order to obtain the two dimensional surface current vector as shown schematically in Figure 6. The total surface current vector estimates is formed by combining the radial vector estimates in overlapping cells associated with a pair of CODAR stations.

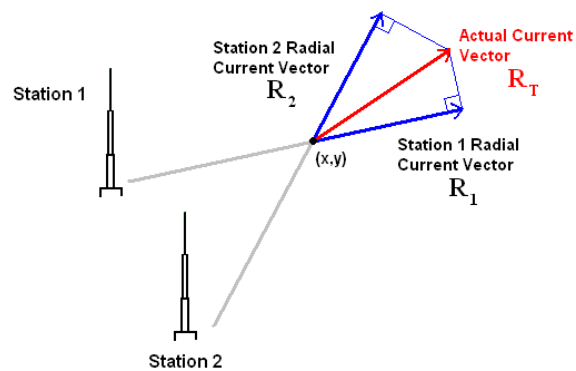


Figure 6. The two radial current estimate vectors (\mathbf{R}_1 , \mathbf{R}_2) which are projections of the total surface current vector (\mathbf{R}_T) along the axis of the radials from their respective stations.

Analytically, each radial current vector ($\mathbf{U}_{r1}, \mathbf{U}_{r2}$) is a projection of the total current vector (\mathbf{U}_T) on the axis along the radial at each point. Since the angles (θ_1 and θ_2) and magnitudes ($|\mathbf{R}_1|$ and $|\mathbf{R}_2|$) of the radial vectors are known (Figure 7) we can define two relations

$$\begin{aligned}\cos(\theta_T - \theta_1) &= \frac{|\mathbf{U}_{r1}|}{|\mathbf{U}_T|} \\ \cos(\theta_2 - \theta_T) &= \frac{|\mathbf{U}_{r2}|}{|\mathbf{U}_T|}.\end{aligned}\quad (4a)$$

Solving for the unknown θ_T and $|\mathbf{R}_1|$ gives

$$\frac{|\mathbf{U}_{r1}|}{\cos(\theta_T - \theta_1)} = \frac{|\mathbf{U}_{r2}|}{\cos(\theta_2 - \theta_T)}.$$

Expanding denominators via trigonometric identity gives

$$\frac{|\mathbf{U}_{r1}|}{\cos \theta_T \cos \theta_1 + \sin \theta_T \sin \theta_1} = \frac{|\mathbf{U}_{r2}|}{\cos \theta_2 \cos \theta_T + \sin \theta_2 \sin \theta_T}$$

which are inverted and rearranged

$$\frac{\cos \theta_1}{|\mathbf{U}_{r1}|} \cos \theta_T + \frac{\sin \theta_1}{|\mathbf{U}_{r1}|} \sin \theta_T = \frac{\cos \theta_2}{|\mathbf{U}_{r2}|} \cos \theta_T + \frac{\sin \theta_2}{|\mathbf{U}_{r2}|} \sin \theta_T \quad (4b).$$

Collecting terms gives

$$\left(\frac{\sin \theta_1}{|\mathbf{U}_{r1}|} - \frac{\sin \theta_2}{|\mathbf{U}_{r2}|} \right) \sin \theta_T = \left(\frac{\cos \theta_2}{|\mathbf{U}_{r2}|} - \frac{\cos \theta_1}{|\mathbf{U}_{r1}|} \right) \cos \theta_T$$

From which we can compute

$$\begin{aligned}\tan \theta_T &= \frac{\sin \theta_T}{\cos \theta_T} = \frac{\left(\frac{\cos \theta_2}{|\mathbf{U}_{r2}|} - \frac{\cos \theta_1}{|\mathbf{U}_{r1}|} \right)}{\left(\frac{\sin \theta_1}{|\mathbf{U}_{r1}|} - \frac{\sin \theta_2}{|\mathbf{U}_{r2}|} \right)} \\ \theta_T &= \tan^{-1} \left[\frac{\left(\frac{\cos \theta_2}{|\mathbf{U}_{r2}|} - \frac{\cos \theta_1}{|\mathbf{U}_{r1}|} \right)}{\left(\frac{\sin \theta_1}{|\mathbf{U}_{r1}|} - \frac{\sin \theta_2}{|\mathbf{U}_{r2}|} \right)} \right]\end{aligned}\quad (4c).$$

$|\mathbf{U}_T|$ can be computed according to

$$|\mathbf{U}_T| = \frac{|\mathbf{U}_{r1}|}{\cos(\theta_T - \theta_1)} \quad (5a)$$

or

$$|\mathbf{U}_T| = \frac{|\mathbf{U}_{r2}|}{\cos(\theta_2 - \theta_T)} \quad (5b).$$

The resultant total vector (surface current vector) is

$$\vec{\mathbf{U}}_T = u_T \vec{\mathbf{i}} + v_T \vec{\mathbf{j}} \quad , \quad (6)$$

where the components are

$$u_T = |U_T| \cos \theta_T \quad (7a)$$

$$v_T = |U_T| \sin \theta_T \quad (7b).$$

The above does not take into consideration the uncertainty of the above “known” measurements.

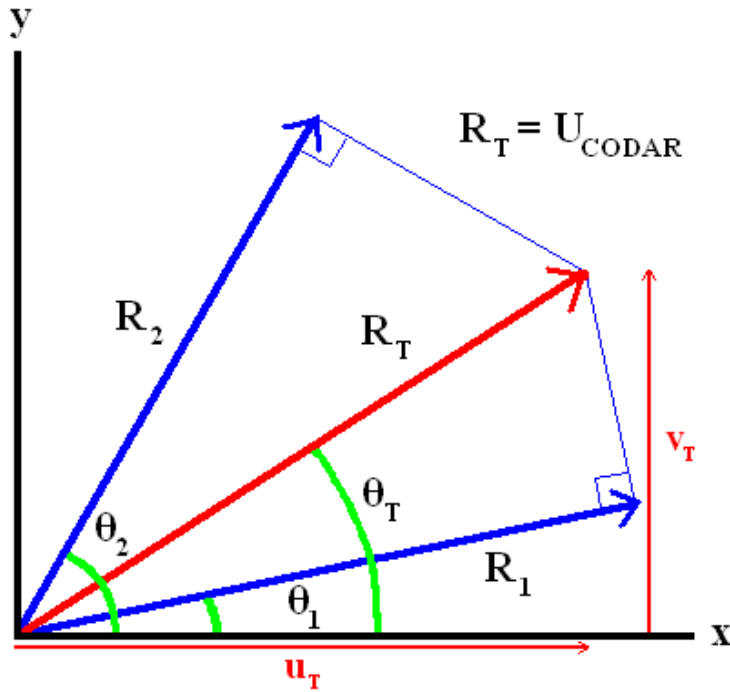


Figure 7. The geometrical relation of two radial vectors (R_1 and R_2 , in blue) to the total current vector (R_T , red).

The angle at which the radials from the two (or more) stations intersect must be large enough so that an accurate estimation of the current’s vector (magnitude and direction) can be made. The closer the relative angle of the two radials is to ninety degrees, the lesser the uncertainty in estimating the orthogonal components of the surface current vector in a rectangular or polar grid. In addition, the points at which the current is estimated for both of the stations do not quite match spatially. The accuracy of $[\theta_2 - \theta_1]$ or $[(\theta_2 - \theta_T) * (\theta_T - \theta_1)]$ is sensitive to uncertainty in radials.

2. CODAR Derived Surface Current Uncertainty

The uncertainty in CODAR-derived currents is due to the measurement uncertainties and the variability of the oceanographic signal. The measurement-related uncertainties include: (1) the distortion of the signal, (2) signal attenuation, (3) making finite estimates, (4) spatial- and

temporal-averaging, (5) current estimate processing, and (6) approximations in the MUSIC algorithm. The CODAR data-processing software accommodates the directly measured CODAR site receiving antenna beam pattern. In its absence the basic processing of backscattered signals assumes an “ideal” antenna beam pattern (see Appendix A).

The uncertainty due to oceanographic conditions, can be attributed to a variety of causes, including wave state, shallow water wave behavior in the closest range cell(s) and the fact that the effective depth of the CODAR “surface current” is actually about 2.4 meters below the surface (with a 4.8 Mhz signal) which can shift the results dependent on wind conditions in any particular cell due to Ekman flow. The principal oceanographic uncertainties are briefly described next.

(a) Oceanographic and Meteorological Variability: Kohut and Glenn (2003) have shown that the majority of signal distortion is due not to the hardware but to the local environment. When trees, shrubs, or buildings are within a couple wavelengths of the antennae, the antenna beam pattern is distorted relative to the ideal antenna pattern, resulting in inaccuracies in the estimated radial current. Fortunately, these errors can be minimized by measuring the antenna beam patterns with a transponder carried by a boat or on foot and then incorporating the true beam pattern into the surface current algorithm (Kohut and Glenn, 2003).

(b) Signal Attenuation Due to Geometric Spreading: The CODAR signal intensity weakens with distance away from the transmitter due to the increased area of the radar cells (see Figure 5). At distant radar cells the signal is lost in the noise. While reduced backscatter energy may not always cause an increase in uncertainty in the detection of the Doppler shift, it does reduce the range of the CODAR (Essen et al, 2000). One way to reduce attenuation is to locate the antennae as close as possible to the water. This minimizes the distance that the signal propagates over land or through the air as both are much poorer signal conductors than the water (Kohut and Glenn, 2003; Emery et al, 2004).

(c) Spatial- and temporal-averaging: Temporal averaging eliminates short-term current variability of periods less than the averaging time of an hour. Spatial-averaging obscures small scale (relative to cell size) variations in current that could skew the estimates towards being either too high or too low. All of the returns from the area of a single cell over the course of the hour are averaged together into one estimate regardless of when over the hour the returns were recorded with the spatial averaging a result of the nature of the measurement that defines the cell dimensions. In addition to the average current estimate, the standard deviation of all the returns that went into the averaging is also recorded as an estimate of the measurement error. This averaging can be visualized using a particular type of CODAR current field map that is normally used to quickly monitor the sites and diagnose potential problems (Figure 8). For each cell in the current estimate field, there is an arrow showing direction and relative magnitude of the hourly average current in that individual cell. This particular plot color-codes the total standard deviation of the number of Bragg backscattered returns from that particular cell over the averaging period. According to Barrick (2006) the total current variance is:

$$\sigma_T^2 = \sigma_U^2 + \sigma_V^2 \quad , \quad (8)$$

where σ_T is the total standard deviation or statistical uncertainty of the measurement (color coded for each cell in Figure 8), and σ_U and σ_V are the standard deviations of the eastward and northward components of the measurement uncertainty. The component standard deviations are estimated by first considering the standard deviation (σ_r) of each individual radial (Figure 9). It is the standard deviations of the u and v components of the returns (calculated from the standard deviation of the radial current magnitudes r of the returns) that are used by the CODAR software as the values for uncertainty.

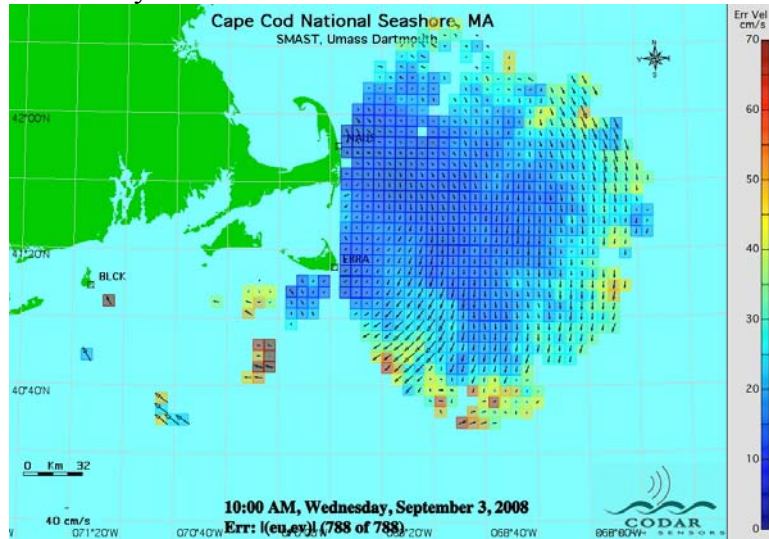


Figure 8. Sample of the display produced every hour with the latest total current estimate field. Current magnitude and direction are shown by the black arrows while the color of each cell shows the standard deviation of the returns that went into the computation of the current estimate at that point.

The CODAR derived surface current components u (lat, lon) and v (lat, lon) include uncertainty data for each point in the velocity field which are the standard deviations (σ_T but given as σ_U and σ_V) of the returns that went into calculating the current estimate at that point (Equations 8-10). In principle, there are 10800 returns that could go into a radial current estimate during the 3-hour averaging period. However, due to limitations of the CODAR measuring system that prevent the detection of more than a couple bearings per range cell per sweep, typically only 30 to 100 returns are more common, with occasional a few vectors formed from 150 returns.

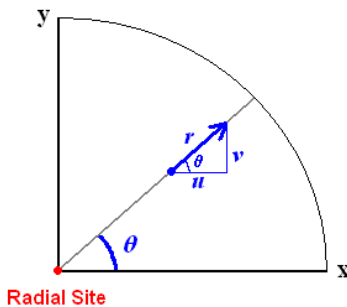


Figure 9. The geometry of a radial current estimate \vec{r} in terms of its (a) polar coordinates - magnitude $|\vec{r}|$ and bearing θ (CCW relative to eastward) and (b) Cartesian coordinates.

The radial current variance is computed according to

$$\sigma_r^2 = \sum_{i=1}^m (|\mathbf{r}_i| - |\bar{\mathbf{r}}_i|)^2 \quad (9)$$

Where \mathbf{r}_i are individual radial current estimates and $\bar{\mathbf{r}}_i$ is the mean. Because the angle (θ) is fixed for a given radial current estimate the σ_u and σ_v components of σ_r can be calculated using the relations

$$\begin{aligned} |\mathbf{r}| &= \mathbf{u}\vec{i} + \mathbf{v}\vec{j}, \\ \mathbf{u} &= |\mathbf{r}| \cos \theta, \\ \mathbf{v} &= |\mathbf{r}| \sin \theta, \end{aligned}$$

and

$$\sigma_r^2 = \sigma_u^2 + \sigma_v^2$$

to obtain

$$\sigma_u^2 = \sum_{i=1}^m \cos^2 \theta (|\mathbf{r}_i| - |\bar{\mathbf{r}}_i|)^2 \quad (10a)$$

$$\sigma_v^2 = \sum_{i=1}^m \sin^2 \theta (|\mathbf{r}_i| - |\bar{\mathbf{r}}_i|)^2 \quad (10b).$$

The Eq(10) variances from one CODAR site are used with corresponding ones for the other CODAR site to estimate σ_u^2 , σ_v^2 and thus σ_T^2 .

(d) *Shallow Water Wave Return Variability*: Processing errors arise from backscattered signals from shallow water waves. The speed of waves in shallow water differ from the assumed stable deep water wave speed (Barrick, 2005). The shallow water induced changes to the Bragg peaks cause the algorithm to overestimate the radial currents. This type of error depends on the frequency of the transmitted radar signal with the lower frequencies having the greatest potential for error. Thus for a 4.8MHz CODAR station, the signal would be affected in regions with a water depth of less than fifteen meters. The great variability of the sea floor causes difficulty in altering the signal processing programs to account for this error.

(e) *Geometric Dilution of Precision (GDOP)*: The geometric dilution of precision (GDOP) is caused by the geometrically fixed but changing angle between the two radials at any given point. The closer the angle is to 90°, the more precise the current estimate. However the uncertainty approaches infinity as the radials from two sites radials become more parallel. GDOP amplifies the uncertainty σ_T in Eq(8) of the radial current component estimate in determining the components of the total surface current vector according to Chapman et al (1997) according to

$$\sigma_n / \sigma_T = \left[2 \left(\frac{\sin^2 \theta_T \sin^2 \left(\frac{\theta_2 - \theta_1}{2} \right) + \cos^2 \theta_T \cos^2 \left(\frac{\theta_2 - \theta_1}{2} \right)}{\sin^2 (\theta_2 - \theta_1)} \right) \right]^{1/2} \quad (11a)$$

$$\sigma_e / \sigma_T = \left[2 \left(\frac{\cos^2 \theta_T \sin^2 \left(\frac{\theta_2 - \theta_1}{2} \right) + \sin^2 \theta_T \cos^2 \left(\frac{\theta_2 - \theta_1}{2} \right)}{\sin^2 (\theta_2 - \theta_1)} \right) \right]^{1/2}, \quad (11b)$$

where σ_n and σ_e are the standard deviations of the northward and eastward components of the total current vector estimate. To obtain the northward and eastward components of the current estimate, multiply the current uncertainty (σ_U or σ_V) by the respective GDOP factor ($\sigma_{n\text{ or }e}/\sigma_T$). For example, the GDOP uncertainties of the respective eastward and northward current components

$$\sigma_{mU} = \frac{\sigma_e}{\sigma_T} \sigma_U$$

$$\sigma_{mV} = \frac{\sigma_n}{\sigma_T} \sigma_V$$

are shown in Figure 10 for our study region.

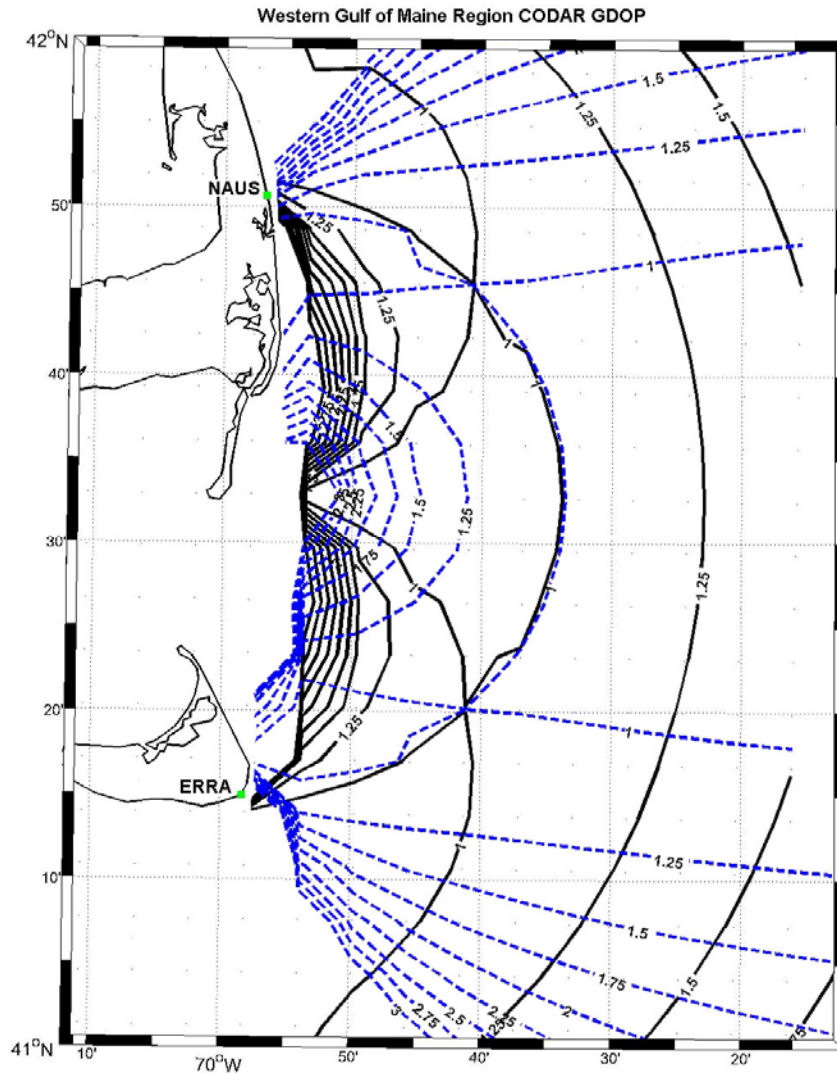


Figure 10. Contour plot of the (GDOP error coefficients for northward (black) and eastward (blue dashed line) components of the total surface current vector derived from the Nauset (NAUS) and Nantucket (ERRA) CODAR sites. The uncertainty coefficients are defined by Eqs(11a) and (11b) in main text.

(f) *Sea-State*: Oceanographic related CODAR uncertainty can arise from an increase in the sea state related noise from which the backscattered signal must be extracted. The Figure 9 example shows a case in which the shorter of the two Bragg peaks nearly disappears (Figure 11). Essen et al (2000) attributed this to the minimal or no resonance that appears in the returned signal when the waves needed for measuring the current are too short in comparison to the Bragg wavelength (30m at 4.8MHz). While high sea states can cause too much noise, Essen et al (2000) also points out that low sea states can also result in the lack of a distinct second Bragg peak. Additional errors from low sea states include measurements that are more affected by interferences such as heavy ship traffic.

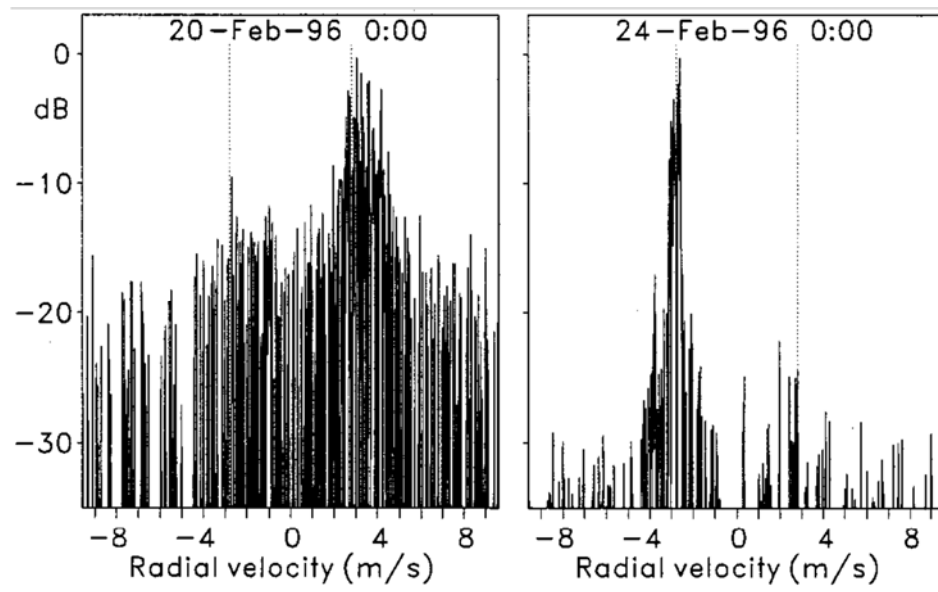


Figure 11. Doppler spectra of backscattered returns from the same $\sim 3 \times 3$ km (25 Mhz signal) ocean patch that is 15km range during (left) high sea state with significant wave heights exceeding 4m and (right) low sea state with waves less than 0.5m from the cell. Note the lack of a second distinct Bragg peak on both images. (Essen et al, 2000)

Drifter Simulation Using CODAR Surface Current Estimates: Ullman et al. (2006) compared several methods of simulating surface drifter trajectories with actual surface drifter measurements. They used CODAR current estimate fields with the basic STPS algorithm to model the trajectories of theoretical drifters in the regions of Block Island and the New Jersey shelf with CODAR measurements. This trajectory was then differenced with actual drifter trajectories over time to obtain an estimate used to choose a search area. Their results showed that the drifter trajectories could be simulated with an uncertainty of less than 20km after 24 hours. This was better than the 45km uncertainty in the USCG method or even the nearly 30km obtained by using the STPS forecasting. It must also be noted that CODAR is the only method that cannot be forecasted as it requires the actual current estimates for each time step while all the others including STPS can predict the future currents.

Here we evaluate the uncertainty of CODAR-derived surface current estimates east of Cape Cod in the Great South Channel a region of particularly strong tidal currents (Brown, 1984). Brown

and Yu (2006) have shown that the regional surface currents besides being strong ($O 1$ m/s) include the formation and movement of significant eddy motion every half semidiurnal tidal cycle (e.g., Figure 12).

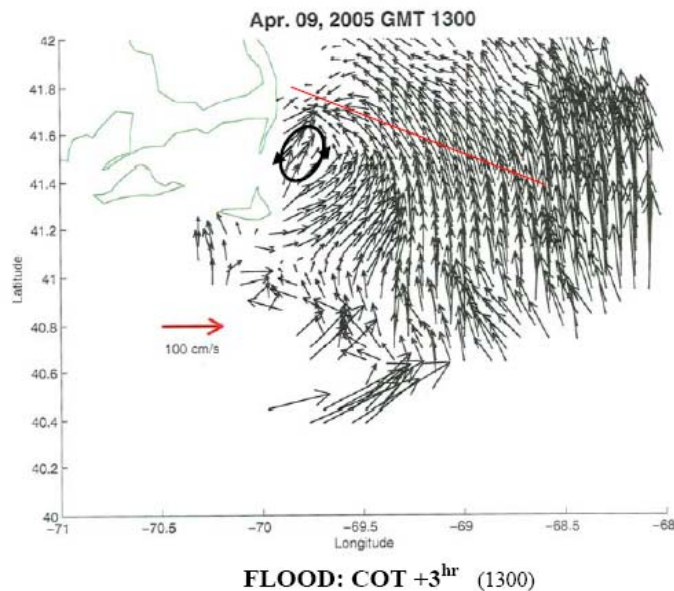


Figure 12. An example of tidal eddy motion is indicated in a CODAR-derived surface current map in the study region. Here COT refers to the change of tide from ebb to flood currents. (Brown and Yu, 2006)

Our objective is to determine the uncertainty of simulating surface drifters using CODAR derived surface currents in the western Gulf of Maine. To do so, we use CODAR measurements to estimate Eulerian surface current fields and surface drifters to estimate Lagrangian surface currents. We compare with observed drifter trajectories with model drifter trajectories using CODAR-derived current field following Ullman et al. (2006)'s use of the basic STPS algorithm in the Western Gulf of Maine.

This study was conducted within the context of a 2008-09 observational/modeling investigation of transient tidal eddy motion in the western Gulf of Maine (see Brown & Marques, 2012; <http://www.smast.umassd.edu/OCEANOL/tte.php>). That study's field program included the collection of CODAR surface current maps, shipboard hydrography and ADCP profiles, and moored ADCP/bottom pressure records were obtained for the study of the tidal eddy motion off of Chatham, MA near the elbow of Cape Cod (Figure 13). These data were collected in May 2008, when the water column is strongly stratified, and during winter 2008-2009 when the water column was well mixed. I focused my study during the January to February 2009 winter period.

Our research measurements included a Davis type surface drifter deployment during the winter 2009. Segments of this drifter trajectory are compared with CODAR derived theoretical surface drifter trajectories. The general drifter simulation model (Equations 1-3) was used to obtain theoretical drifter trajectories using CODAR derived surface currents (see http://www.smast.umassd.edu/OCEANOL/reports/TTE/CODAR_WINTER08-09_dataRPT_30apr09.pdf). Sets of model drifter trajectories were compared to each of the

surface drifter segments in order to obtain information on the uncertainties in simulating surface drifter trajectories in the Gulf of Maine region and the role of oceanography and tidal eddies on surface drifters.

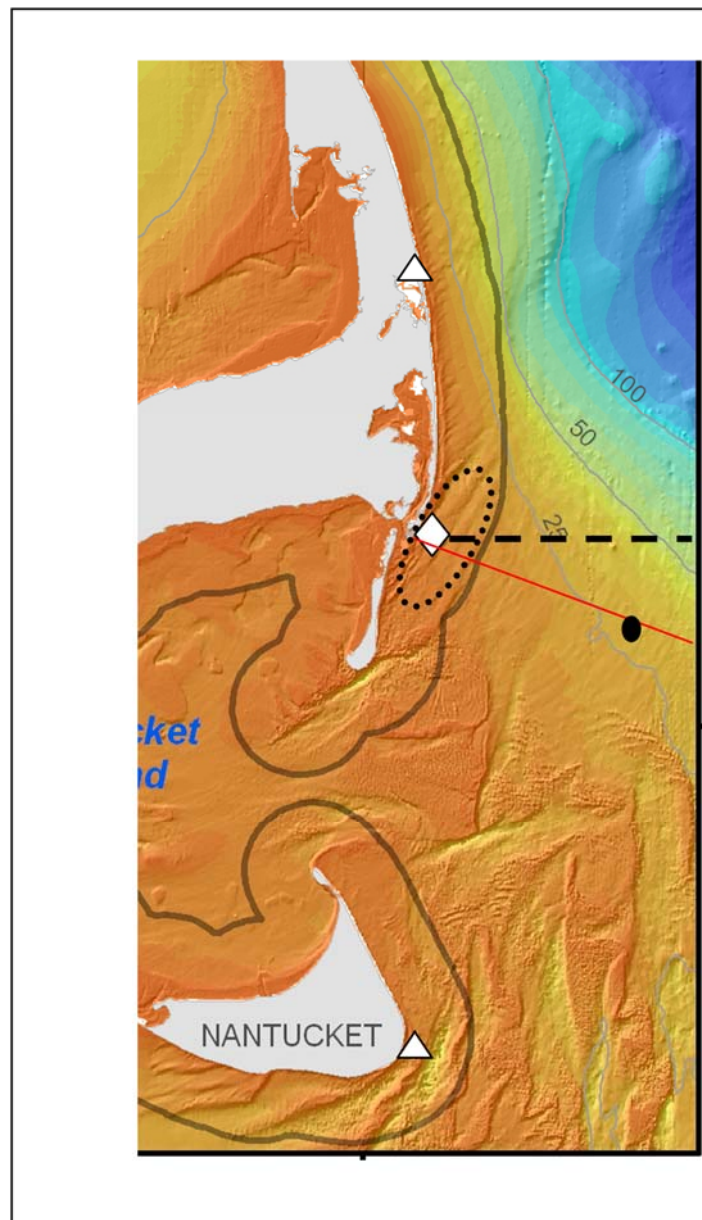


Figure 13 (right) The site of the field measurement program consisting of CODAR sites (triangles) at Nauset and Nantucket, a shipboard water property and ADCP profile transect (black dashed), bottom-mounted ADCP/pressure 30m mooring site (diamond); and the NSD mooring site (solid oval); all relative to the site of eddy motion generation (dotted). A reference transect (solid red) overlays the regional bathymetry (Courtesy of B. Butman, USGS).

2. MEASUREMENTS

2.1 Drifter Measurements

The Davis-type drifter (Figure 14) used in this study was designed by Jim Manning (NOAA-NMFS Woods Hole, MA) and built by Univ. of Southern Maine students working with the GoM Lobster Foundation, Kennebunk, ME; and manufactured by students working with. The drifter had two 1m^2 sails with floats that were attached so as to keep the sails right below the surface. The GPS unit mounted on the drifter was originally designed for the trucking industry and use the GLOBALSTAR satellite system. The drifter was programmed to record its location using GPS every 35 minutes, the shortest time step available to the GPS units used in order to maximize the amount of data available.



Figure 14. Images of the Davis-style drifters used for this experiment. Each of the four individual sails is approximately $1\text{m} \times 0.5\text{m}$ and is attached to floats to keep it at the surface; the thin box on the top of the central mast contains the GPS unit. (second photo from Manning et al, 2009)

Our drifter (No. 91191), which was released at 1603 GMT on January 27, 2009 off of Chatham, Massachusetts at approximately 41.68°N and 69.78°W . This location was chosen to maximize the amount of time possible for it to remain in the CODAR coverage region based on the behavior of previous drifters deployed by Jim Manning. The drifter continued transmitting until March 25, 2009 (see Figure 15). While CODAR-derived current maps were available for almost all of the drifter deployment, the regional velocity coverage was highly variable. The CODAR-drifter current comparison was also confounded due to a poorly understood malfunction in which the time intervals between drifter GPS fixes varied between 11 minutes and 20 hours. Still we were able to identify five useable drifter segments during which CODAR-derived surface current coverage was reasonable .

To standardize comparisons between drifter 91191 segment trajectories and CODAR-derived drifter trajectories, a maximum Δt of approximately three hours for drifter time intervals was chosen. By using this time interval as a filter, five segments of the drifter 91191 trajectory (Figures 16 and 17) with (a) a length of at least five hours and (b) adequate CODAR current coverage (see Figure 20) were identified (see Figure 21; Table 1; and Appendix C for details).

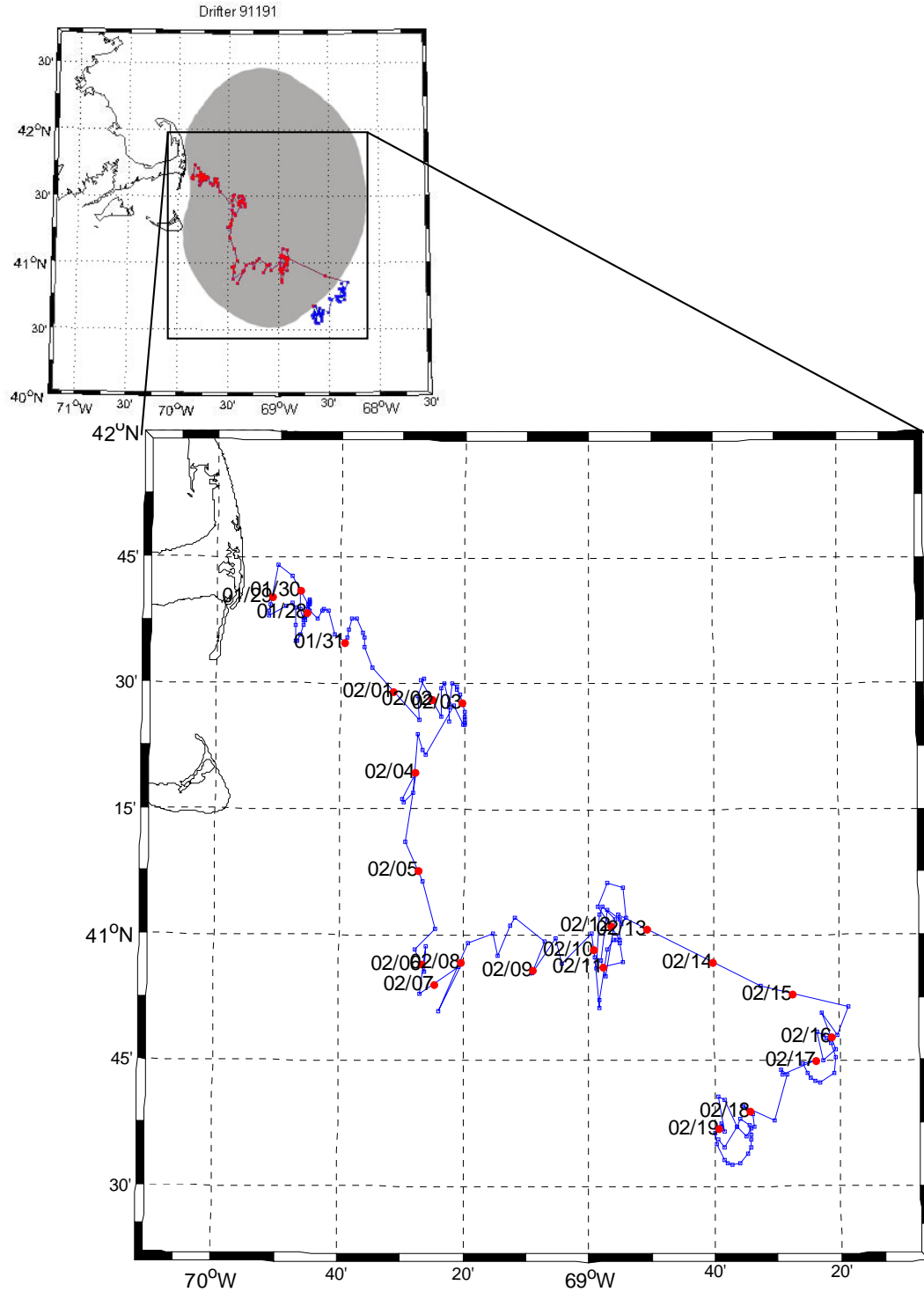


Figure 15. (below) Surface drifter trajectory from January 27, 2009 to February 19, 2009. Red dots indicate the daily drifter position at 0000 GMT. Blue points indicate drifter position for each fix recorded (bottom). (above) Red points show drifter locations within the ideal CODAR coverage region (grey area). CODAR current estimates are available for the entire deployment period.

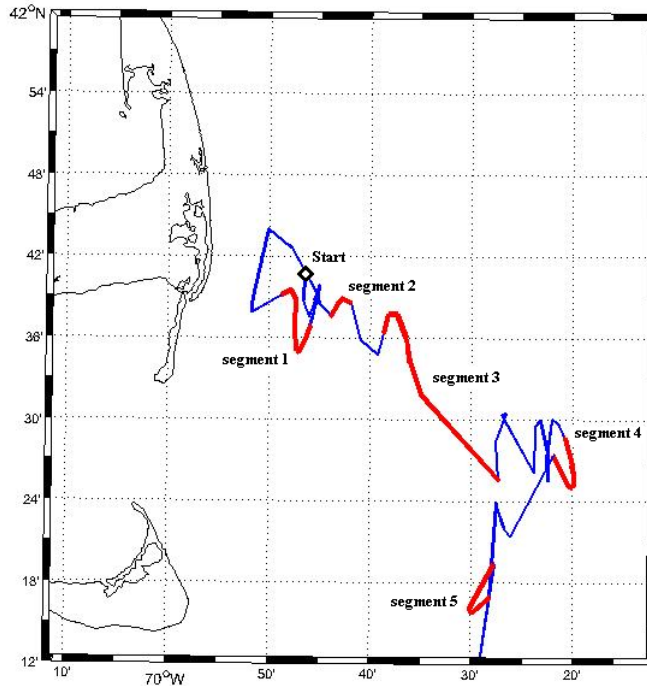


Figure 16. Portions of the drifter's track that are useful for comparing to theoretical drifters. Sections were chosen where the time intervals between fixes are comparable to those of opportunistic drifters.

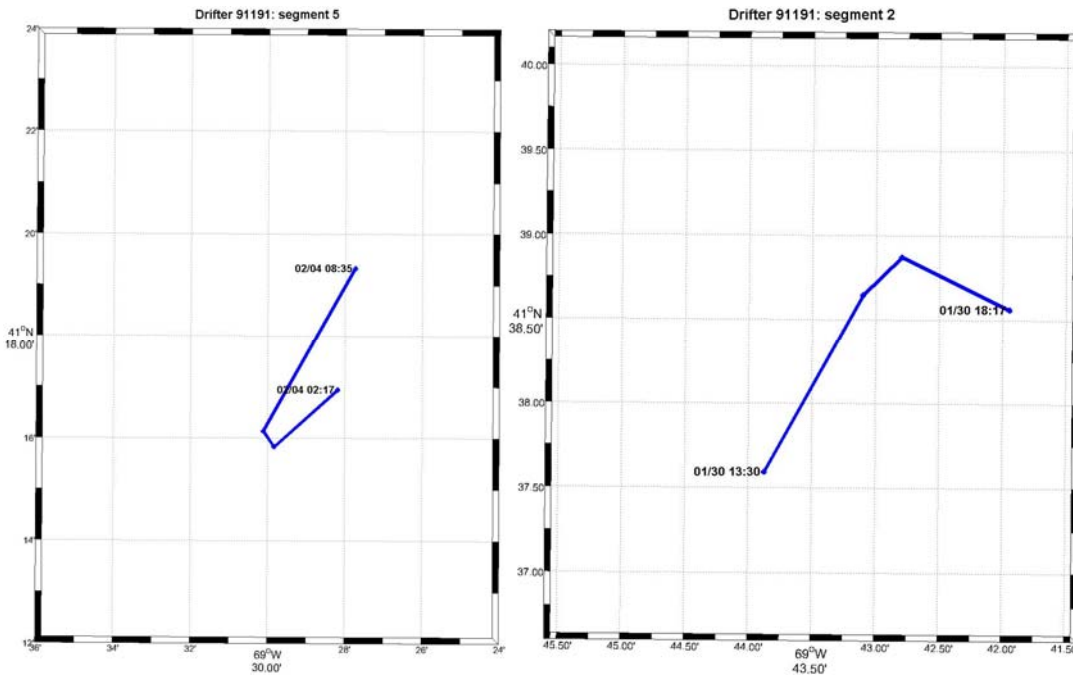


Figure 17a. Drifter 91191 track segments (above left) 1 and (above right) 2.

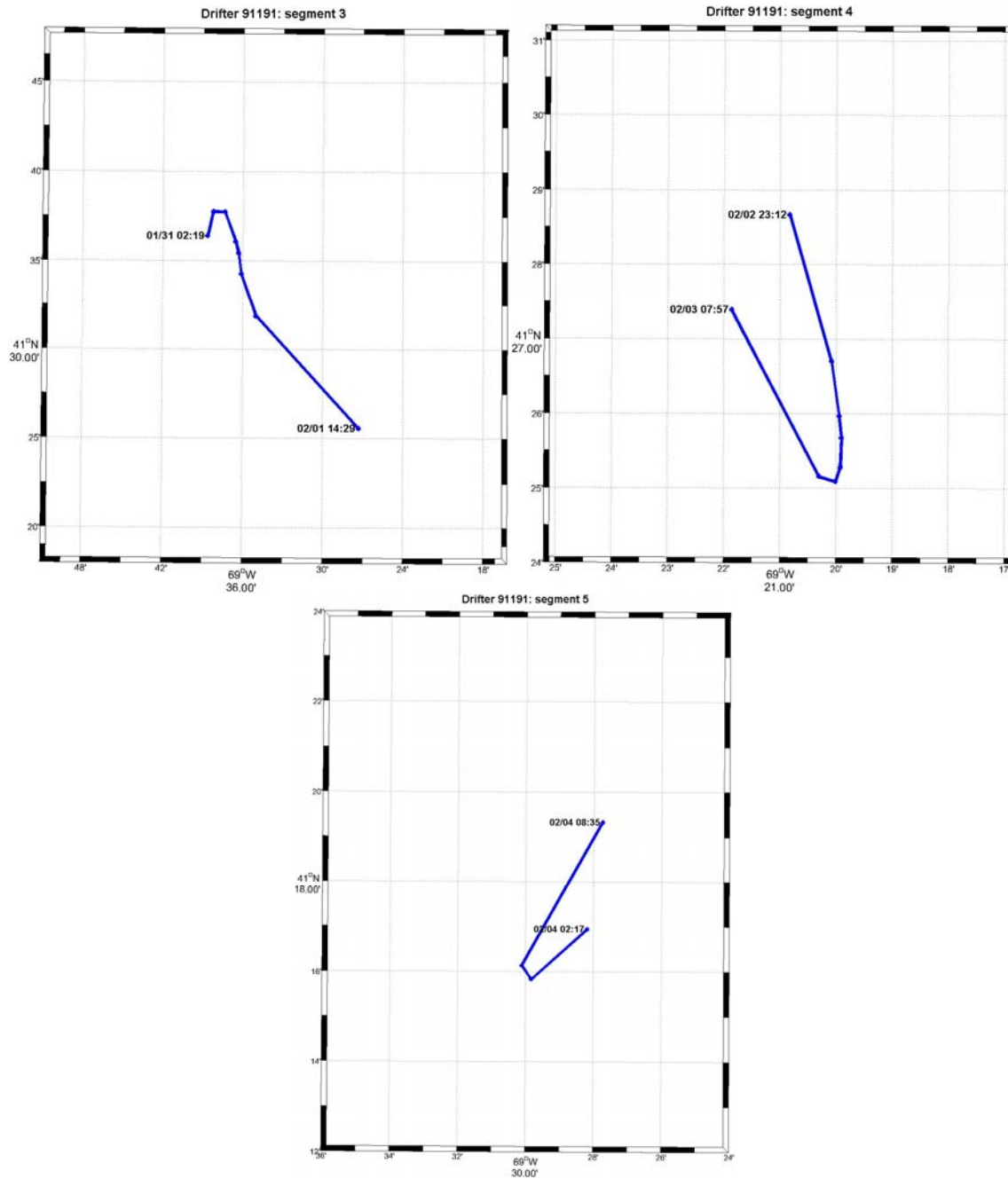


Figure 17b. Drifter 91191 track segments (above left) 3, (above right) 4 and (below) 5).

Table 1. Time ranges of CODAR maps used for the observed and CODAR derived drifter trajectory analysis for the different segments used for drifter simulations. Note that CODAR End is the time of the last CODAR file used when calculating the segment, one hour prior to the end time of the segment calculations. See Appendix C for the drifter trajectory time series.

<i>Segment</i>	<i>CODAR Start (GMT)</i>	<i>CODAR End (GMT)</i>	<i>Length (hours)</i>	<i>Drifter Start (GMT)</i>	<i>Drifter End (GMT)</i>	<i>Min. drifter dt</i>	<i>Max. drifter dt</i>
<i>1</i>	1/28/09 0700	1/28/09 1600	10	0640	1651	00:40	02:00
<i>2</i>	1/30/09 1300	1/30/09 1800	6	1330	1817	00:25	02:25
<i>3</i>	1/31/09 0200	1/31/09 1400	13	0219	1429	00:22	02:55
<i>4</i>	2/03/09 0000	2/03/09 0700	8	2313	0757	00:11	03:32
<i>5</i>	2/04/09 0200	2/04/09 0800	7	0217	0835	00:47	04:10

2.2 CODAR Surface Current Measurements

Two CODAR installations provided surface current maps for the study region, one was the Nauset site at the Cape Cod National Seashore in Eastham, Massachusetts and is run by the University of Massachusetts Dartmouth while the other is on Nantucket and is run by Rutgers University (Figure 18). CODAR radial current data was collected from both the Nantucket and Nauset CODAR stations and combined using the system manufacturer’s (SeaSonde) software to obtain current vector field estimates.

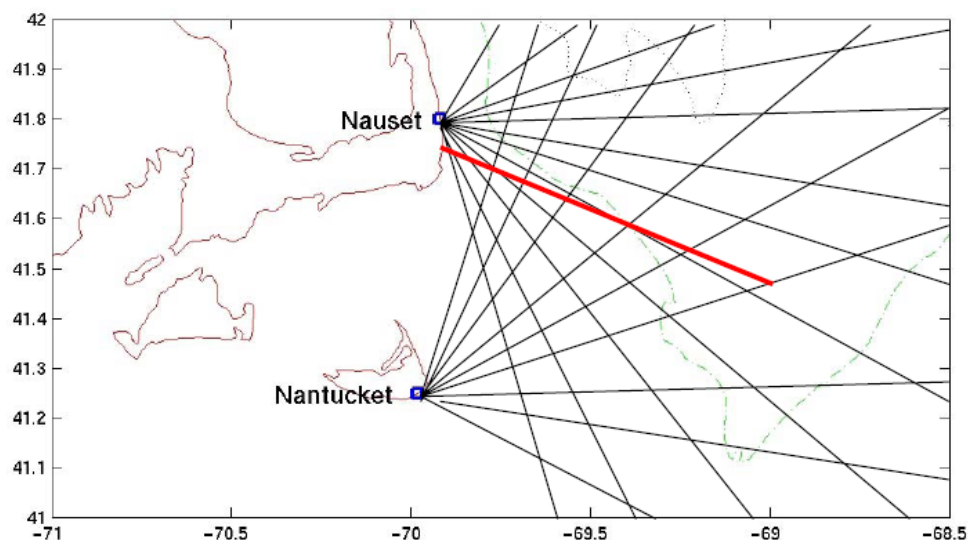


Figure 18. Locations of the two CODAR sites used for this project. Red line is used for reference. (Brown and Yu, 2006)

Hourly current maps (Figures 19a-f) relevant to the drifter trajectory segments were then produced by combining the radial currents from each of the two sites according to Eq 7 (see http://www.smast.umassd.edu/OCEANOL/reports/TTE/CODAR_WINTER08-09_dataRPT_30apr09.pdf for the more complete set).

The total current field maps produced includes the latitude, longitude, u and v components of velocity as well as the standard deviations (σ_u and σ_v from Equations 8-10) of the returns that went into calculating the u and v components respectively for each point in the field which is based on a rectilinear grid given by the CODAR system with approximately 6km between points which is determined by the size of the range bins of the radial sites (5.8 km at 4.8 MHz). Due to variations in the CODAR coverage region, there are often points on the grid without current estimates. Linear interpolation is used to fill in gaps in the coverage region. See a selected subset of CODAR derived current maps in Appendix B.

WSB: You will need to locate the NSD and NSA sites in at least one of the in each of the following Figure 15 clusters so as to facilitate your discussion of the oceanography –i.e tidal variability as presented in the NSD and NSA timeseries- during each segment.

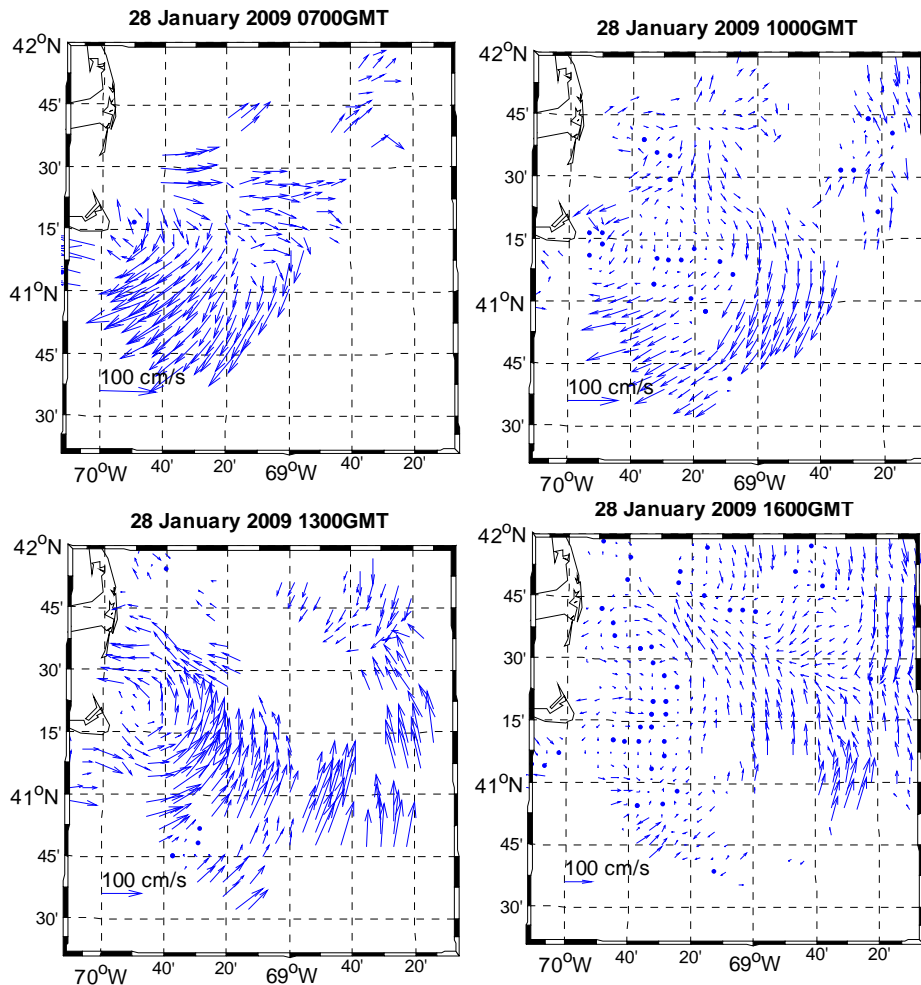


Figure 19a. Examples of surface current maps obtained using CODAR current estimates from the Nauset and Nantucket sites for drifter segment 1.

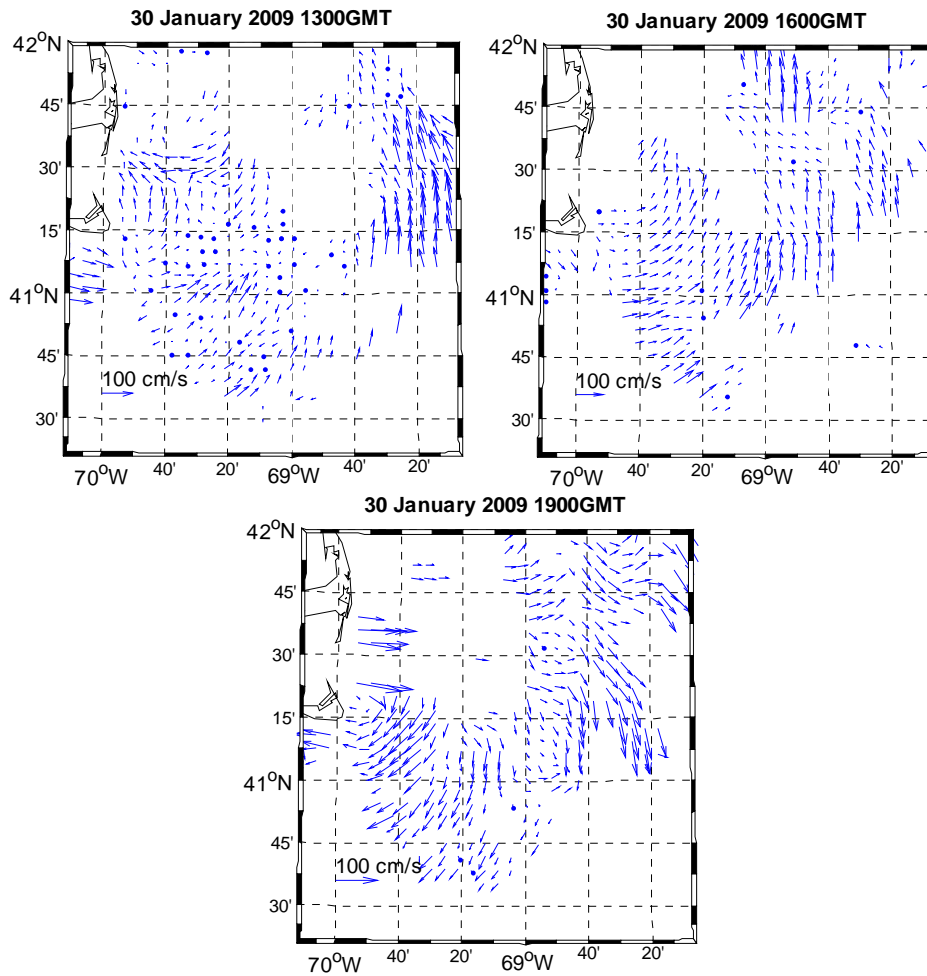


Figure 19b. Examples of surface current maps obtained using CODAR current estimates from the Nauset and Nantucket sites for drifter segment 2.

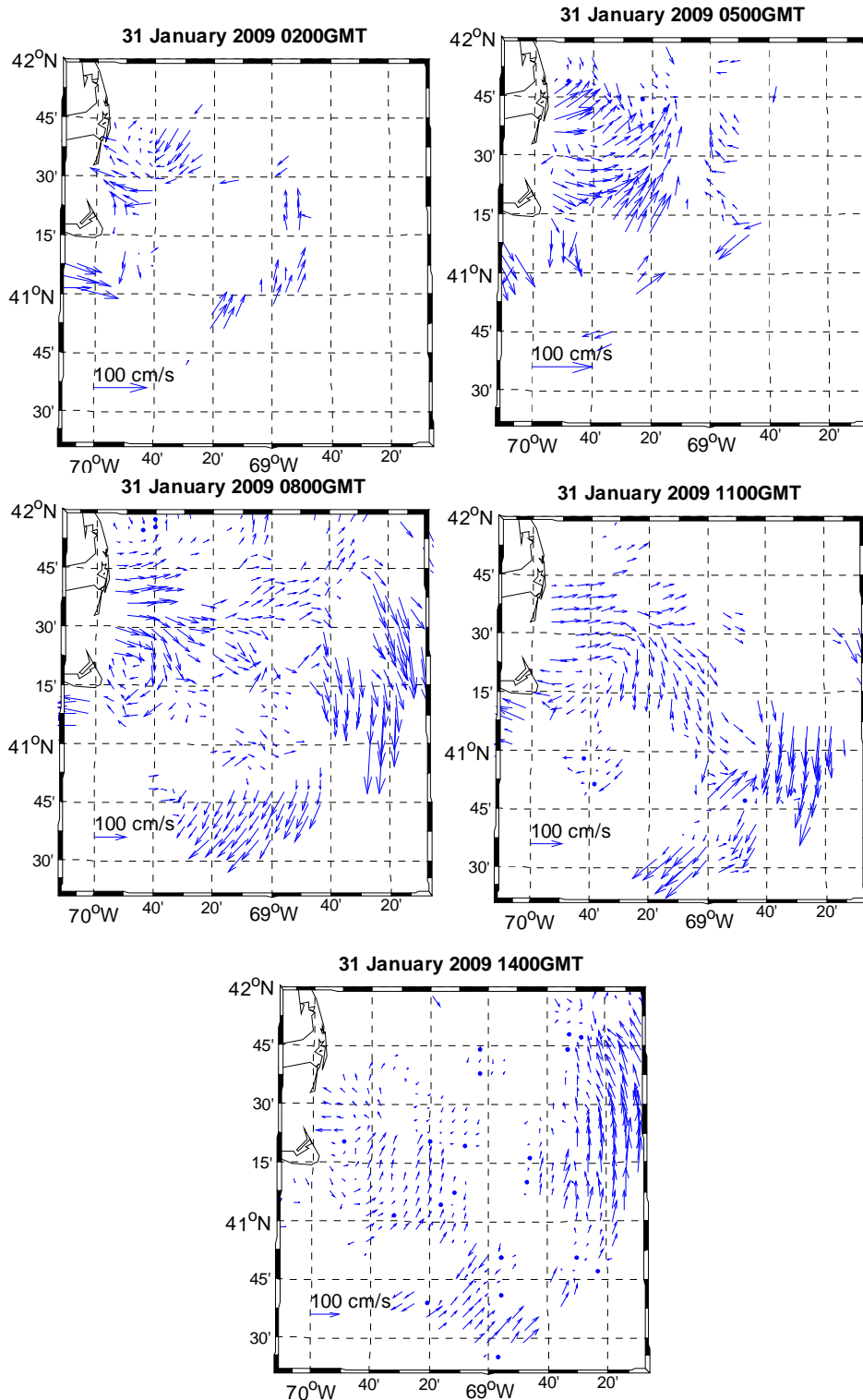


Figure 19c. Examples of surface current maps obtained using CODAR current estimates from the Nauset and Nantucket sites for drifter segment 3.

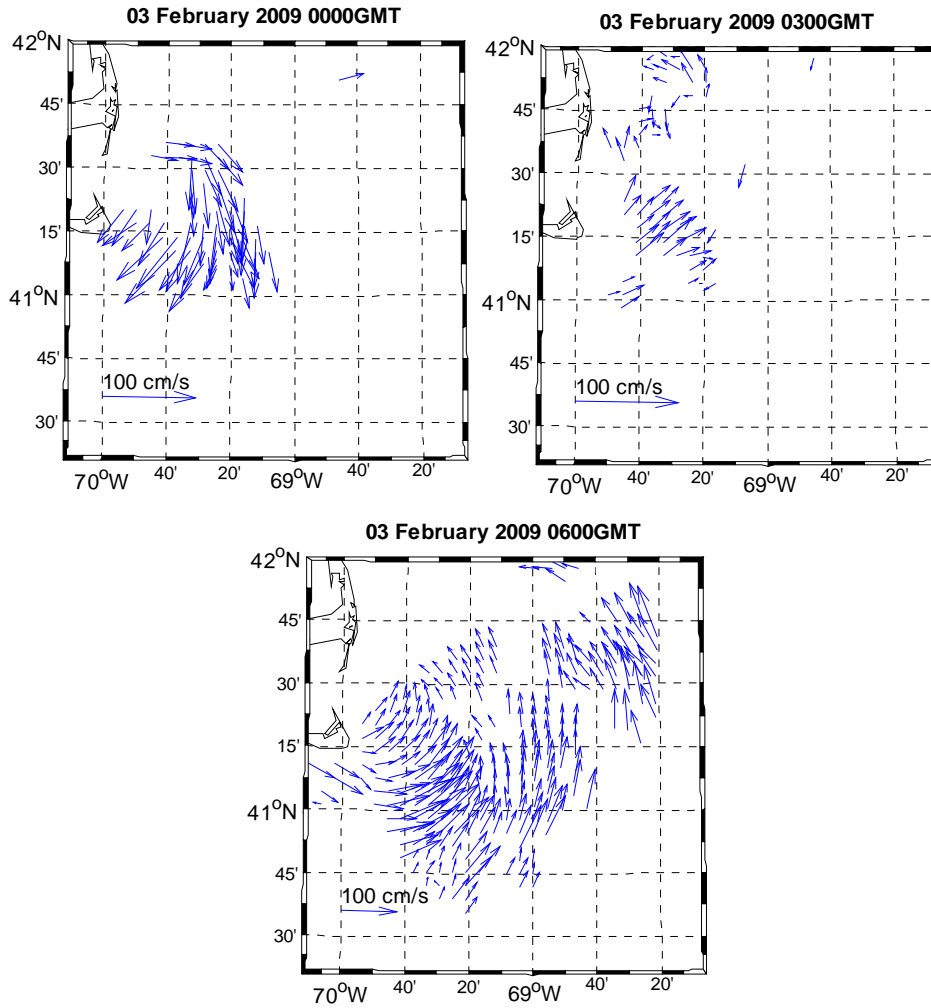


Figure 19d. Examples of surface current maps obtained using CODAR current estimates from the Nauset and Nantucket sites for drifter segment 4.

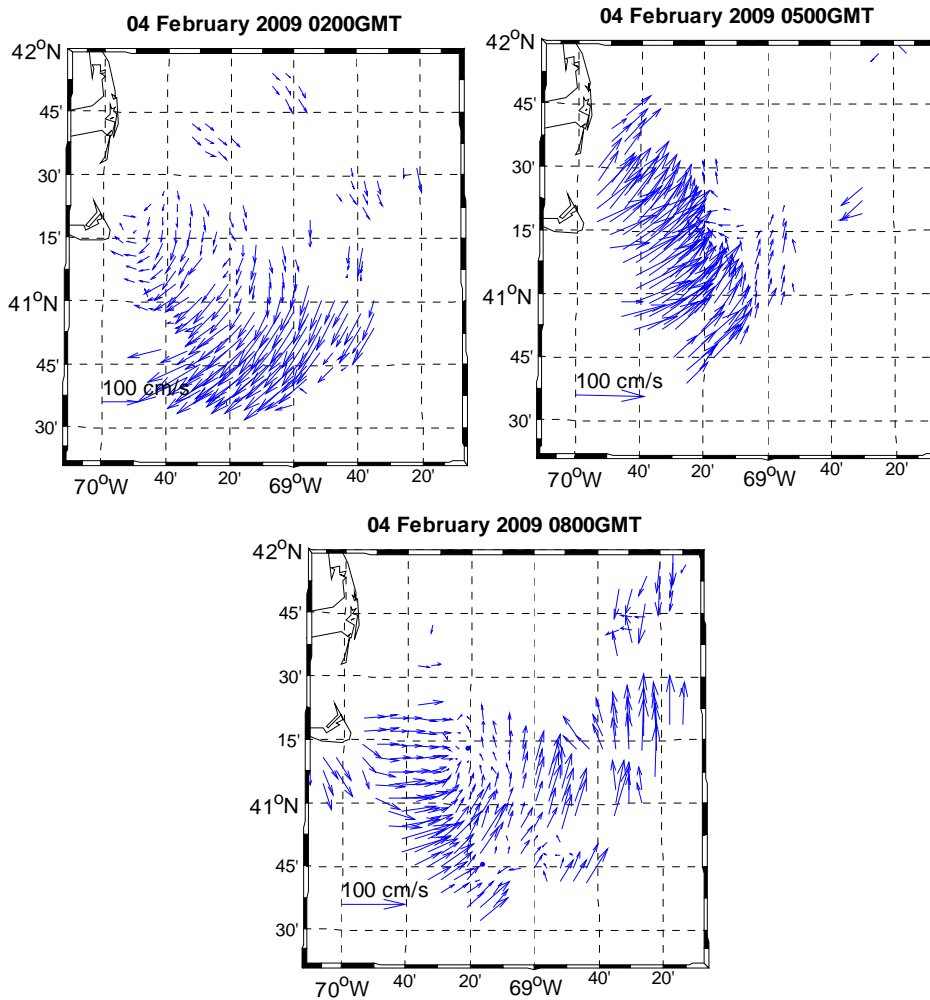


Figure 19e. Examples of surface current maps obtained using CODAR current estimates from the Nauset and Nantucket sites for drifter segment 5.

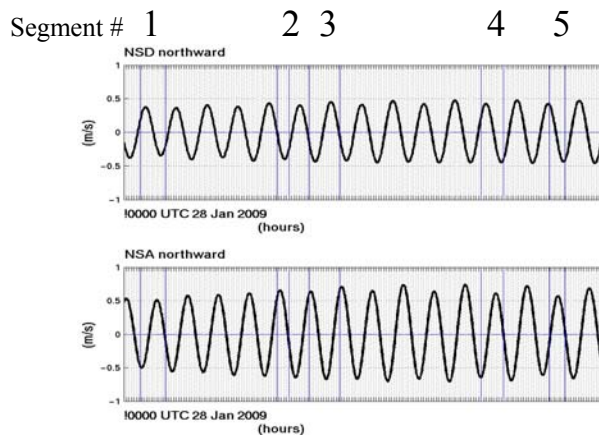


Figure 20. Predicted northward currents at sites NSD and NSA, with drifter segments defined. Note that NSD is closer to the drifter in segments 1 and 2 while NSA is closer to segments 3, 4 and 5.

Segments 1, 2, 4, and 5 start during ebb tide with predominately southward flow and feature a change from ebb to flood tidal flow. Segment 3 features both a change from ebb to northward flowing flood and flood to ebb. Segments 2 and 5 currents are weaker because they start shortly before the change of tide (Figures 19b and 19e). For both 2 and 5 the majority of the segment is during flood tide while the other segments include both ebb and flood tidal flow with flood currents most going northward. Flow separation with eddy motion formation, such as is described by Brown and Yu (2006), is likely to have occurred near shore during all or some of these scenarios shown in the current maps (Figures 19a-19f). (WSB: Shawna is there any evidence of eddy motion in Fig 15?)

2.3 Model Drifter Trajectories via CODAR Measurements

For the initial set of model drifter trajectory runs, the velocity fields from the CODAR u and v current estimates were used with Equation 3 with the uncertainty $u' = 0$; which under these circumstances reduced to $u = U_{radar}$. The model drifter trajectory (without uncertainty) was constructed as follows. The initial conditions of each model drifter trajectory segment were the start time (t_0), latitude (x_0) and longitude (y_0) of the observed drifter (see the segment initial conditions in Appendix C). The successive hourly segments of the modeled drifter trajectory were computed by substituting U_{radar} for $u(t,r)$ and one hour for Δt equal in Equation 2b. This is justified because the displacements $\Delta r \ll 6\text{km}$. The $\Delta r \ll 6\text{km}$ was an important condition of the calculation because, if Δr was as large or larger than the CODAR cell size, then there would be a need to incorporate additional CODAR current estimates into the estimate of the model drifter location at the end of the hour. Successive segments of the simulated drifter trajectory were obtained similarly. The differences between the modeled and observed drifter trajectories in Figure 22 are inevitable because the velocity estimate used (i.e., U_{radar}) does not include current uncertainty (u') – a topic considered next.

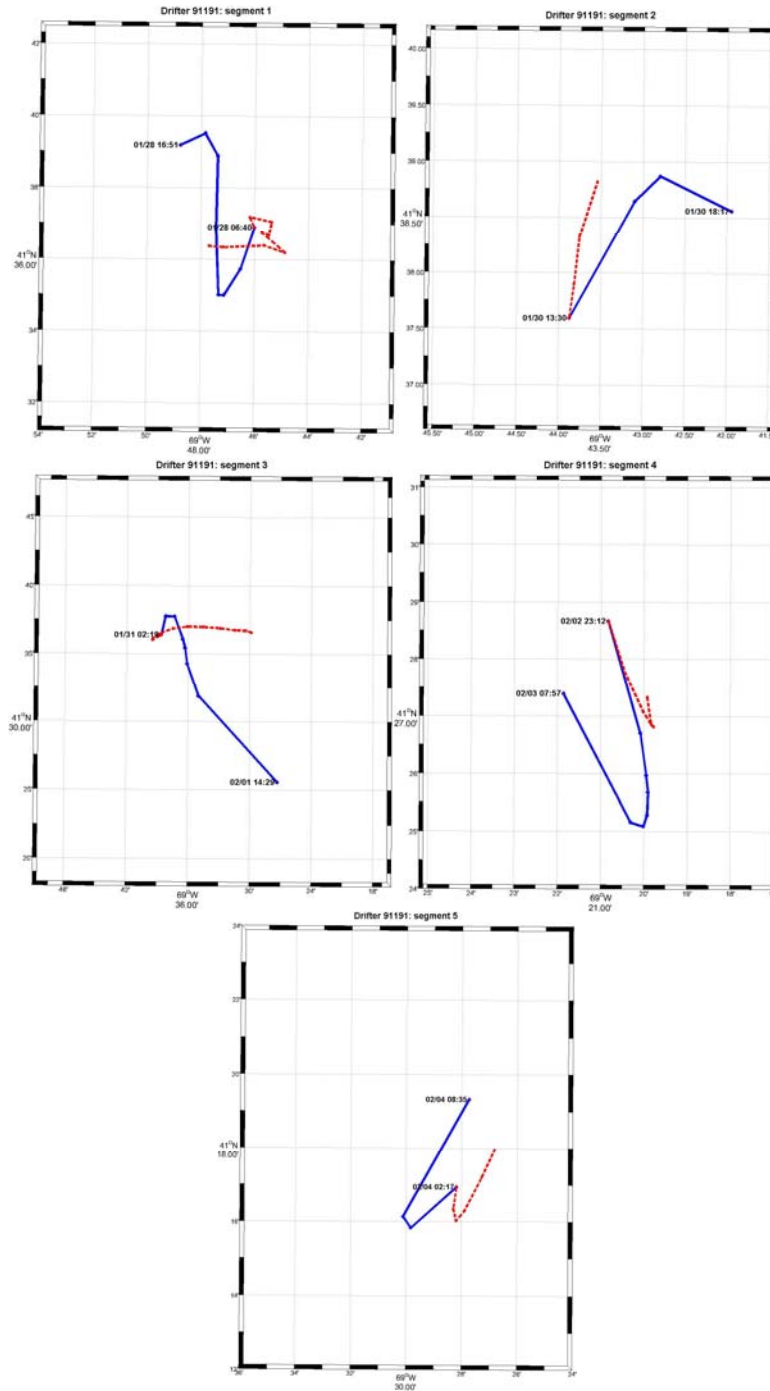


Figure 21. Comparison of observed (blue) and simulated (red) drifter trajectories for each segment. The drifter simulation algorithm (see text) was applied without including allowances for the uncertainty. Each interval between points represents one hour.

Modeled Drifter Trajectories with Uncertainty

The differences between modeled and observed drifter trajectories is explored by considering uncertainty in the model drifter trajectory calculation. The differences between the observed drifter trajectory and multiple realizations of a model drifter trajectory calculation with

uncertainty considerations enable probability estimates of future drifter locations. make it possible to obtain an estimate of the uncertainty in the prediction of a drifter in the water as a function of time. Knowledge of the last known position and uncertainty can be used to better plan a potential search area.

The uncertainty in a model drifter trajectory is related to contribution of the uncertainty in the CODAR surface current estimate (\mathbf{u}') on the the model trajectory calculation.

The CODAR derived velocity \mathbf{U}_{radar} only approximates the true space-time averaged velocity $\mathbf{u} = \mathbf{U}_{radar} + \mathbf{u}'$, -t he difference being the current uncertainty \mathbf{u}' . Ullman et al (2006) use either the random walk or the random flight methodology to model the uncertainty \mathbf{u}' .

The random walk methodology given by

$$\mathbf{u}' = \sigma \frac{\sqrt{T_u}}{\Delta t} \Delta \mathbf{w}, \quad (10)$$

where $\Delta \mathbf{u}'$ σ is the standard deviation of \mathbf{U}_{radar} , Δt is the model computation time step (one hour), $\Delta \mathbf{w}$ is a random Markovian variable with a normally-distributed random increment (with zero mean and a second moment of $\langle \Delta \mathbf{w} * \Delta \mathbf{w} \rangle = 2\Delta t$), σ σ_U σ_V σ_{mU} σ_{mV} and T_u is the time scale which is equal to $\Delta t/2$ for random walk.

The random flight methodology algorithm for $\Delta \mathbf{u}'$ - the fluctuation of the uncertainty velocity \mathbf{u}' - is

$$\Delta \mathbf{u}' = - \frac{\mathbf{u}'}{T_u} \Delta t + \frac{\sigma}{\sqrt{T_u}} \Delta \mathbf{w}, \quad (11a)$$

where T_u is the integral timescale. The time integration of Eq (11a) gives the velocity uncertainty

$$\mathbf{u}' = \mathbf{u}'(t-1) e^{-\Delta t/T_u} + \frac{\sigma}{\sqrt{T_u}} \Delta \mathbf{w} \Delta t \quad (11b)$$

in which we have assumed that $\mathbf{u}'(0) = \frac{\sigma}{\sqrt{T_u}} \Delta \mathbf{w} \Delta t$.

The random flight model also employs a scaled random value like the random walk model but the formula is given as the variation of the velocity error and there is an additional term that introduces “memory” of the velocity of previous time steps. The memory decays with an e-folding time of T_u with the degree of influence of an earlier \mathbf{u}' on later steps diminishing with time (Ullman et al, 2006). This memory term is significant only for short time periods but compared to the random walk model it more accurately approximates the behavior of real drifters where the momentum of the drifter may cause it to briefly move counter to the random turbulent flow (Griffa et al, 1995).

The velocity estimate standard deviation σ can be obtained from the CODAR file (σ_U and σ_V) or better yet after calculating the GDOP (σ_{mU} and σ_{mV}). The integral timescale in both the u and v directions were computed by bin-averaging the velocities of five drifter segments to one hour time intervals and then auto correlating each of the 10 series (see Appendix D).

IV. Results

For each of the five observed drifter trajectory segments, one hundred particle trajectories were computed using the model with both the random walk and random flight uncertainty models with GDOP-related uncertainties included (also see Appendix E). The mean of the model drifter trajectories is quite different than the observed drifter trajectory for segment 1 (Figure 22a). The mean model and observed drifter trajectories in segments 2 (Figure 22b), 4 (Figures 22c), and 5 (Figure 22d) showed similar behavior.

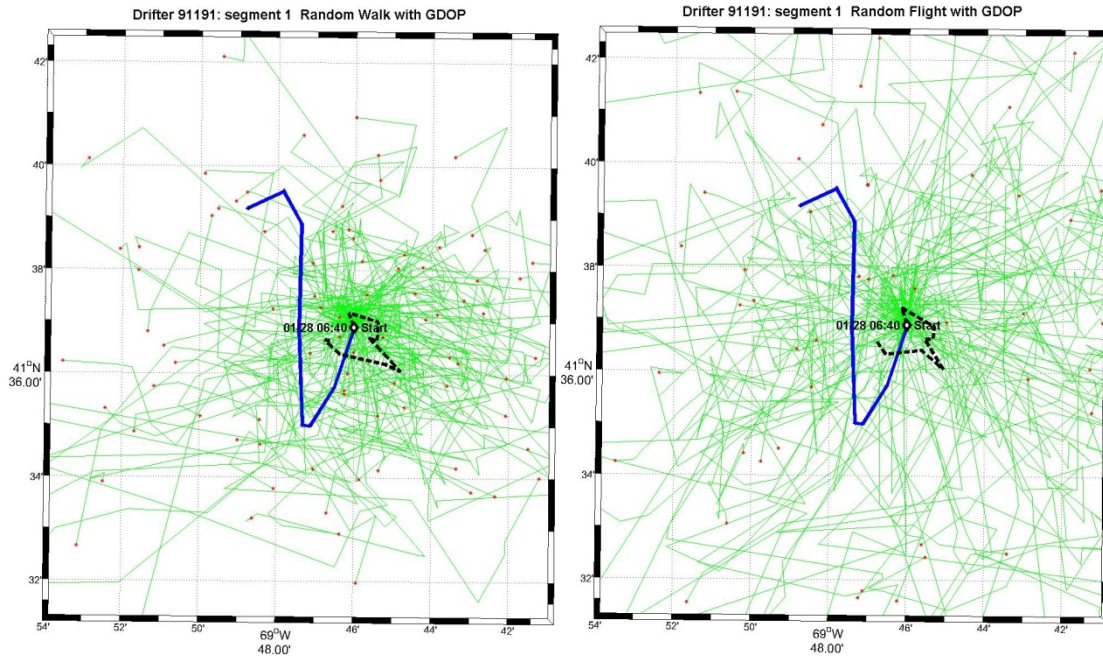


Figure 22a. The set of 100 modeled drifter trajectories (green) for segment 1 observed trajectory (blue solid) and the average model drifter trajectory (black dot) using the random walk model (left) and random flight (right).

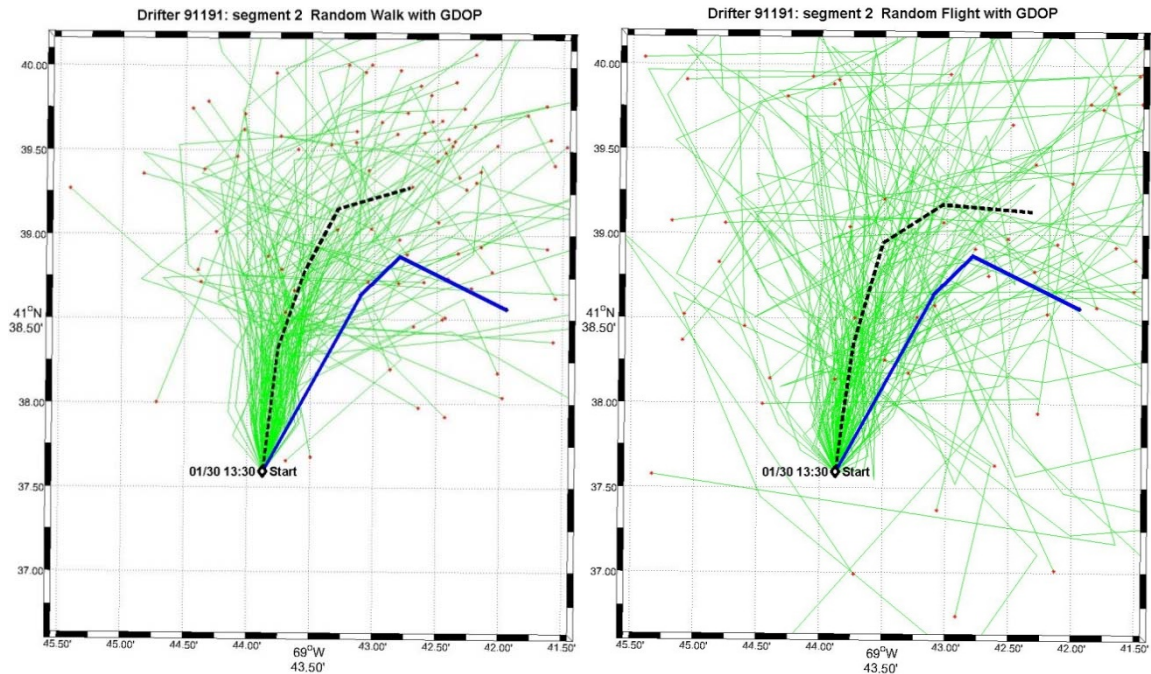


Figure 22b. The set of 100 modeled drifter trajectories (green) for segment 2 observed trajectory (blue solid) and the average model drifter trajectory (black dot) using the random walk model (left) and random flight (right).

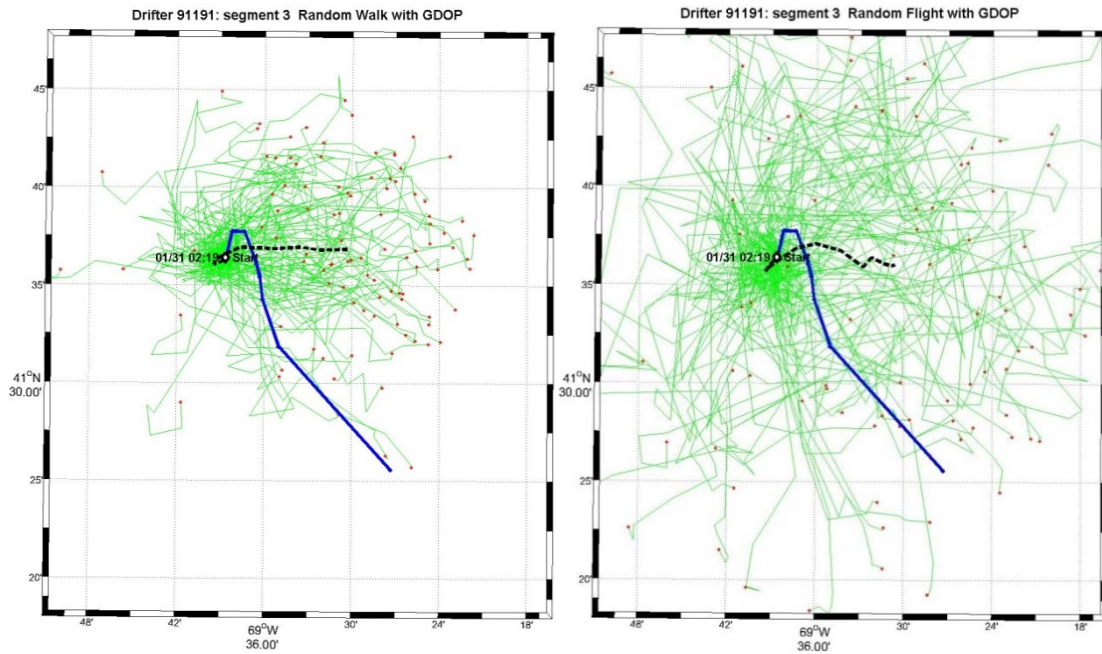


Figure 22c. The set of 100 modeled drifter trajectories (green) for segment 3 observed trajectory (blue solid) and the average model drifter trajectory (black dot) using the random walk model (left) and random flight (right).

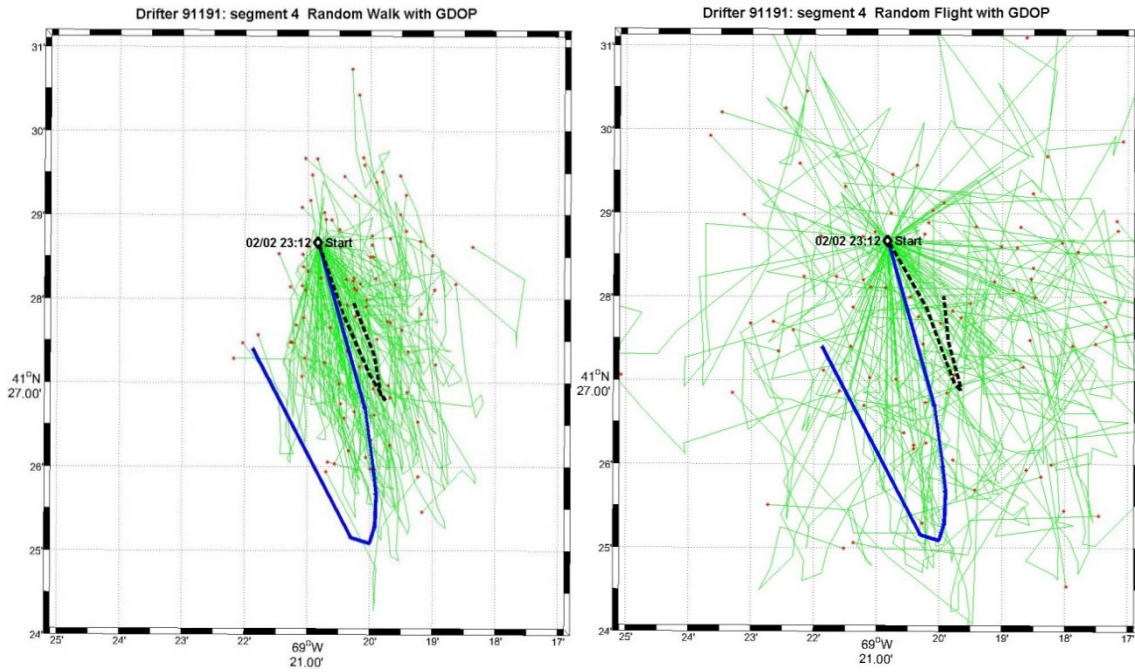


Figure 22d. The set of 100 modeled drifter trajectories (green) for segment 4 observed trajectory (blue solid) and the average model drifter trajectory (black dot) using the random walk model (left) and random flight (right).

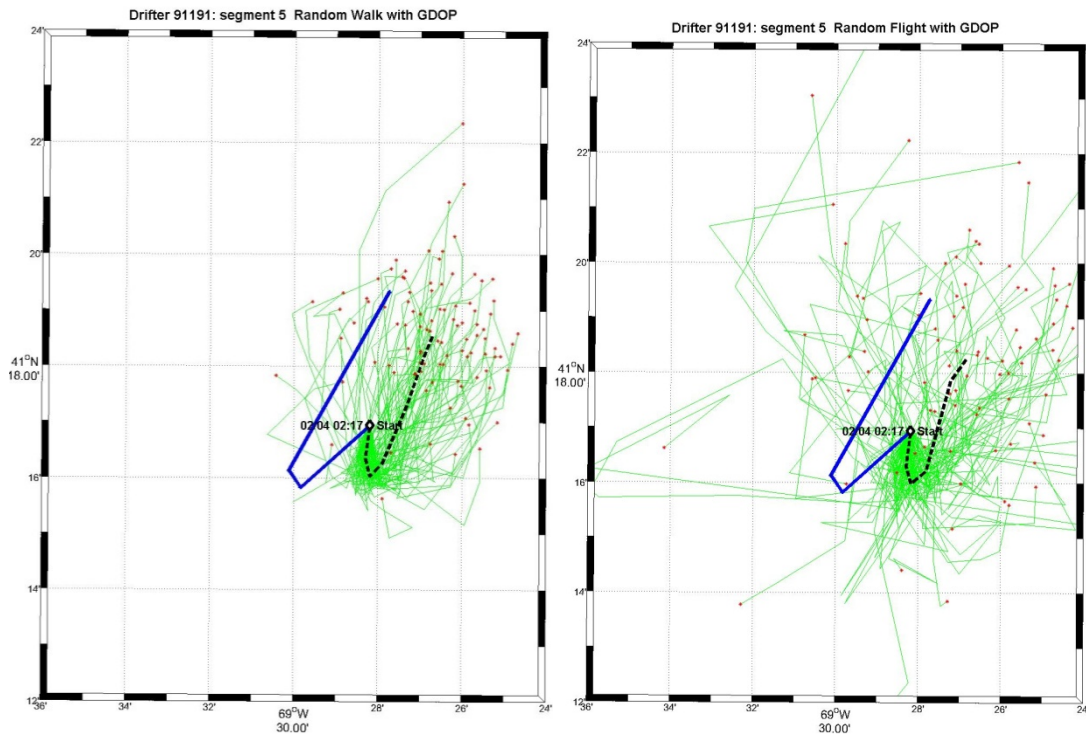


Figure 22e. The set of 100 modeled drifter trajectories (green) for segment 5 observed trajectory (blue solid) and the average model drifter trajectory (black dot) using the random walk model (left) and random flight (right).

Drifter Separation Plotted by Model Type

While the observed surface drifter trajectories reflect the time/space integrated effects of the finer scale ocean current variability, those derived from the CODAR-derived surface currents do less so because of their space- (approximately 6km) and 3-hour time-averaging. Thus comparisons between model drifter trajectories can be expected to provide estimates of such differences. In order to quantitatively compare the observed and model drifter trajectories, I computed the time series of separation distance between the observed and sets of the 100 model drifter trajectories shown in [Figure 22](#).

The time series of separation between each observed drifter segment and the mean or 95th percentile of the respective 100 model drifter sets are shown for both uncertainty model types in [Figures 23a-d](#). One general conclusion is that the observed minus mean model drifter separation time series with the two different uncertainty types have a similar structure; which in the cases of segments 2, 3, and 5 is a near-linear increase with time.

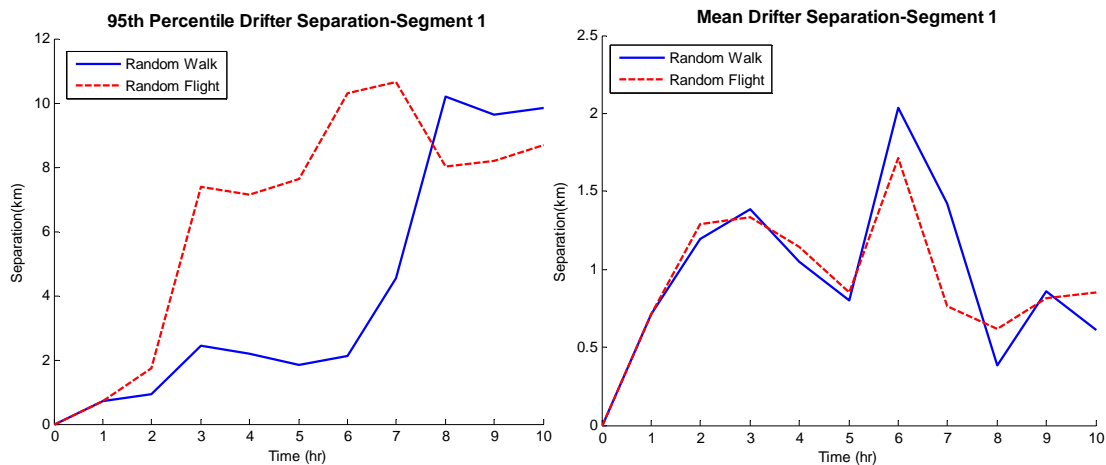


Figure 23a. Segment 1: Time series separation between the observed drifter and (left) 95th percentile model drifter and (right) mean model drifter with both random walk (blue solid) and random flight (red dashed) uncertainty.

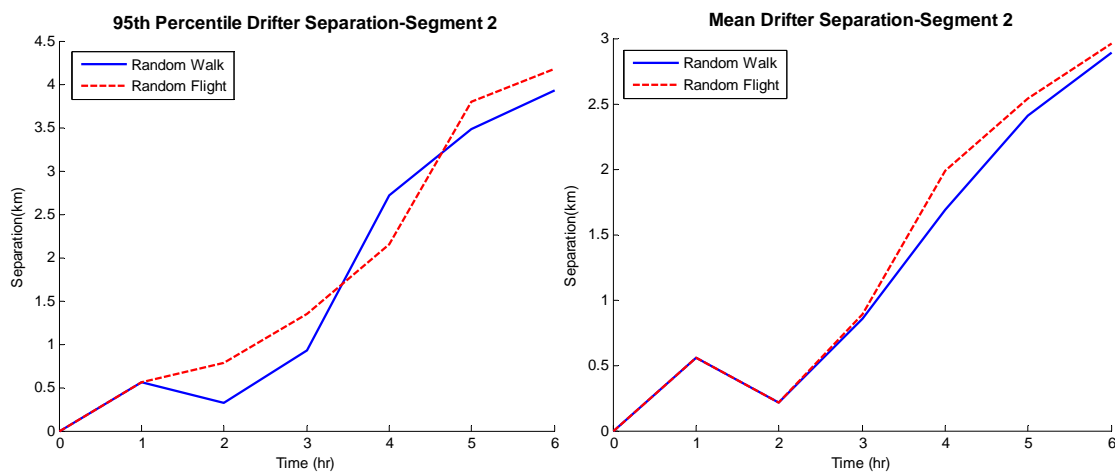


Figure 23b. Segment 2: Time series separation between the observed drifter and (left) 95th percentile model drifter and (right) mean model drifter with both random walk (blue solid) and random flight (red dashed) uncertainty.

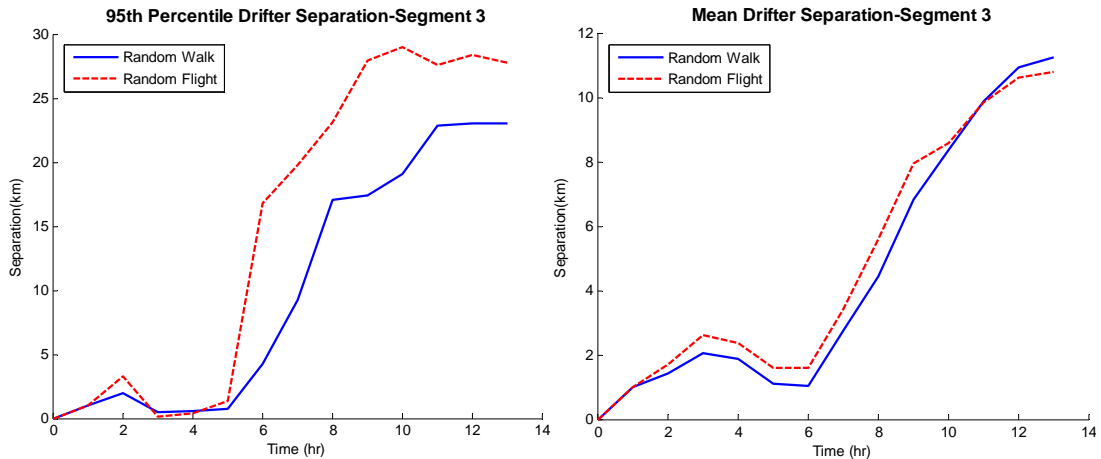


Figure 23c. Segment 3: Time series separation between the observed drifter and (left) 95th percentile model drifter and (right) mean model drifter with both random walk (blue solid) and random flight (red dashed) uncertainty.

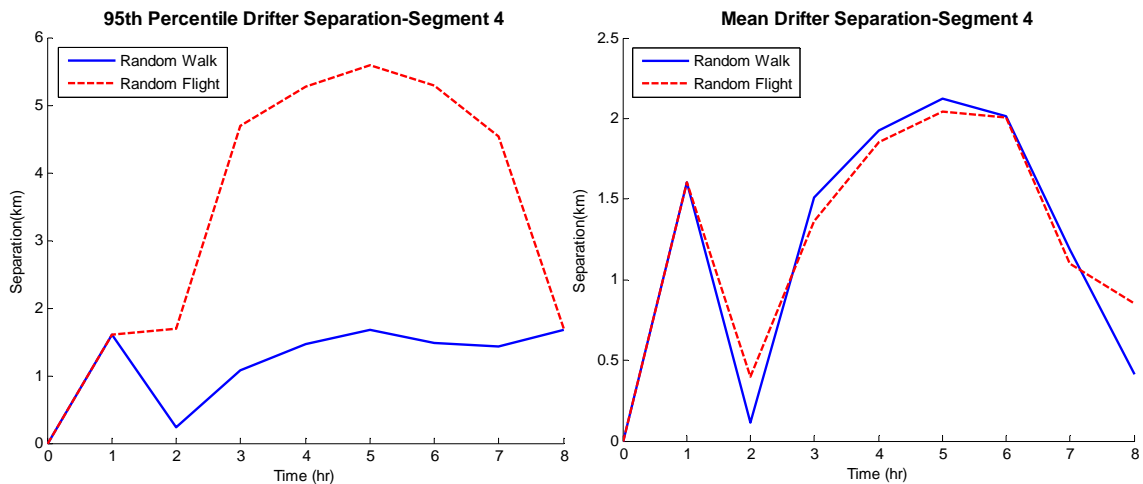


Figure 23d. Segment 4: Time series separation between the observed drifter and (left) 95th percentile model drifter and (right) mean model drifter with both random walk (blue solid) and random flight (red dashed) uncertainty.

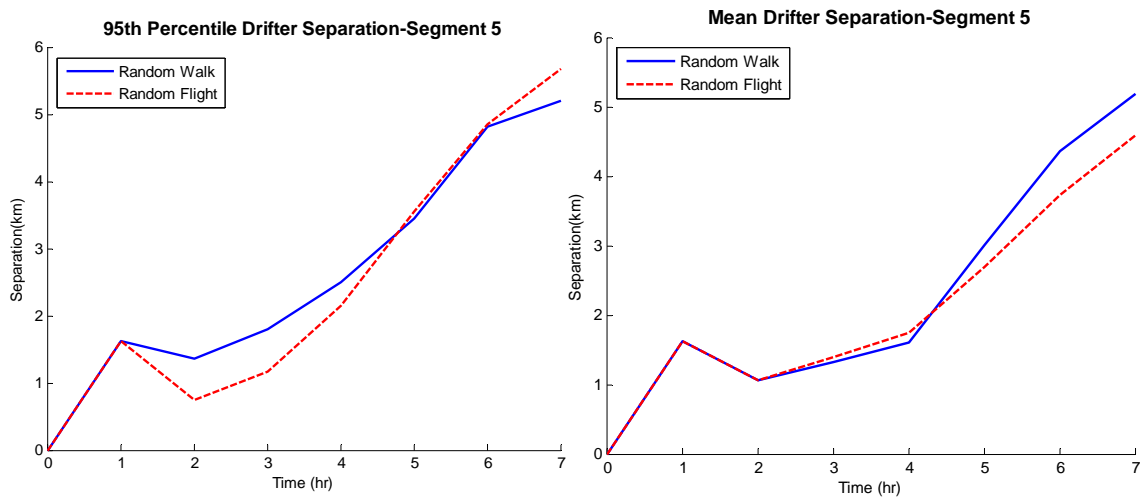


Figure 23e. Segment 5: Time series separation between the observed drifter and (left) 95th percentile model drifter and (right) mean model drifter with both random walk (blue solid) and random flight (red dashed) uncertainty.

Generally, the 95th percentile separations for the first five hours of all segments are similar as shown in Figure 24.

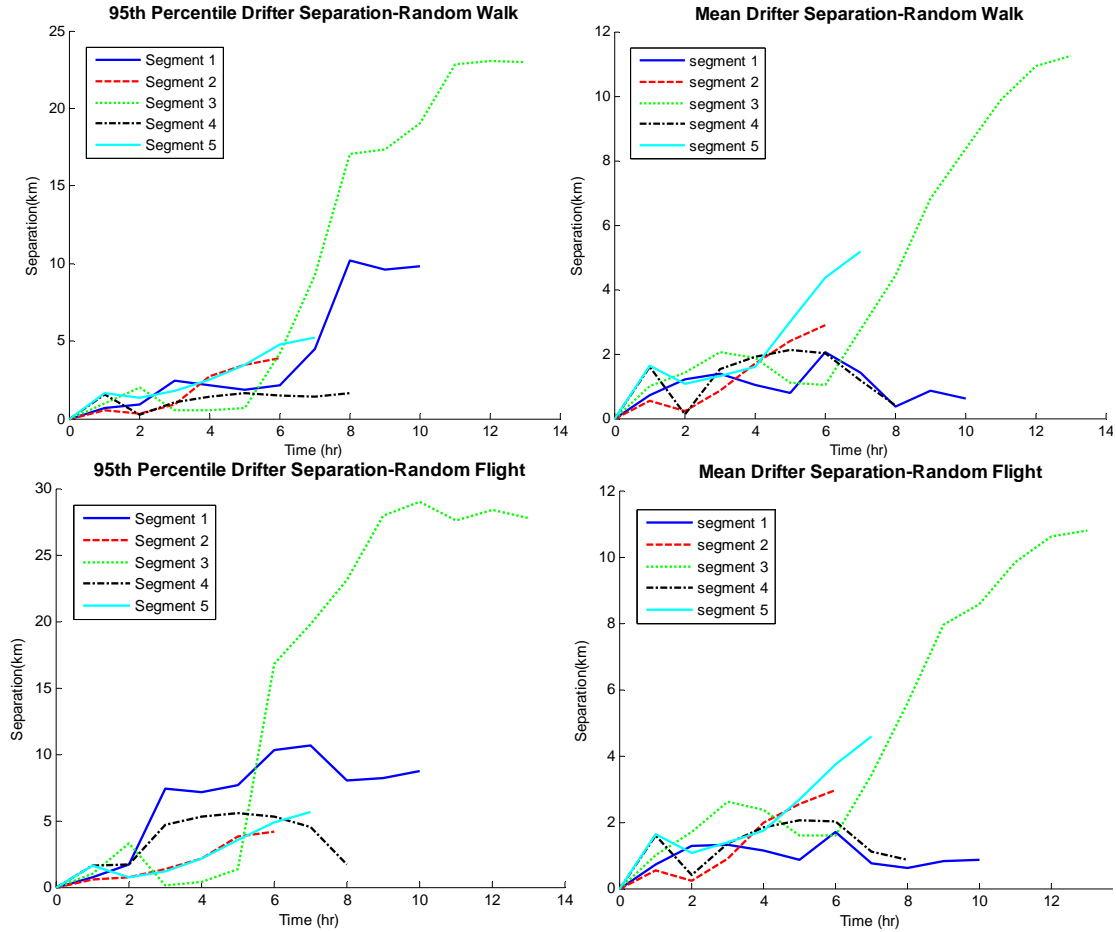


Figure 24. Composite of the time series separation between the observed drifter and (left) 95th percentile model drifter and (right) mean model drifter with both random walk (blue solid) and random flight (red dashed) uncertainty.

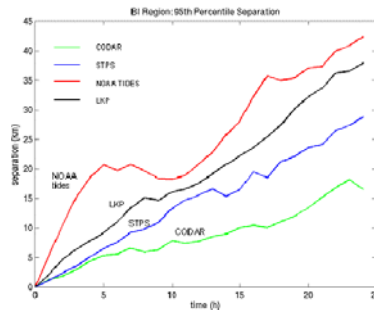


Figure 25. Sample comparison of the 95th percentile separation between actual and predicted drifters as a function of time for the four major models used. (O'Donnell et al, 2006)

WSB: Shawna rather than the following description try to describe these statistical results in terms of the various stages of the tidal cycle (see alternate figure 16 above) in which these segment trajectories are imbedded. I think that comment also applies to your discussion.

The highest separation occurs with segment 3 except for in the random walk model where both segment 1 and segment 3 increase in separation sharply after six hours. Segment 2 is the shortest of all the segments and while the plots of the drifter cluster makes it appear as if it has minimal spread between the modeled drifters, when looking at the separation plots by model type (Figures 23a and b), it is comparable with the other plots. In all of the drifter separation by model type plots all four of the segments show a trend towards increasing separation with time.

Drifter Separation Plotted by Segment

Halfway through both segments, the separation of the models increased quickly. Segment three also shows both the models have nearly identical behavior until the last two hours of the simulation. Unlike with the other segments, segment 4 shows a distinct oscillation in time of the separation between the real and modeled drifters.

WSB: “cone of probability” like with a hurricane...I’m not sure how useful this would be with segments 1 and 4 since #1 appears to be an amorphous cloud and #4 keeps coming back on itself...2 and 3 would probably be okay though

Shawna you had what I think were presentations that approximated what you suggest above. I would include a relevant few if you still have them.

V. Discussion

Initially, both the segment 2 and segment 4 model drifter clusters appeared to be quite similar to the actual drifter path. However, the comparison in Figures 26a and 26b ??? shows that segment 2 is just too short to determine whether or not the simulations were accurate or if it was merely too short a time period for the cluster to spread.

Segment 4 is the farthest from Cape Cod and therefore was less affected by the flow separation during each ebb and flood tide. Thus the surface currents were more tidal as evidenced by the approximate 12-hour oscillation in all the model calculations (Figure 33b ???, bottom). While 91191 shows some tidal oscillation it translates more than forms closed loops like what the CODAR data shows. If the real drifter is moving almost linearly while the ones modeled using CODAR current estimates are traveling in nearly closed loops then it would cause the separation distance to oscillate with an increasing trend as the drifter moves further away from the looping simulation. Since segment 4 of the actual drifter path is not looping it would imply that there is additional surface current flow that was not picked up by the CODAR.

where, the practice is to simulate a set of pseudo-drifters located at the LKP at the start. The result is a cluster of modeled pseudo-drifter trajectories (Figure 22); which when differenced with the “true measured surface drifter trajectory” operationally characterize the uncertainty in the CODAR surface current field as shown in Figures 22a and b. In this model the standard deviation obtained from the CODAR radial current data is multiplied by the square root of the timescale (equal to half the time step for this model) divided by the length of the time step (Δt). Because the velocity fluctuations due to error and small scale variations are assumed to be random, the resultant term is multiplied by the random variable which is an increment that is normally distributed around a mean of zero. This results in a random value for u' scaled to the error in the measurements used to estimate the current in that location.

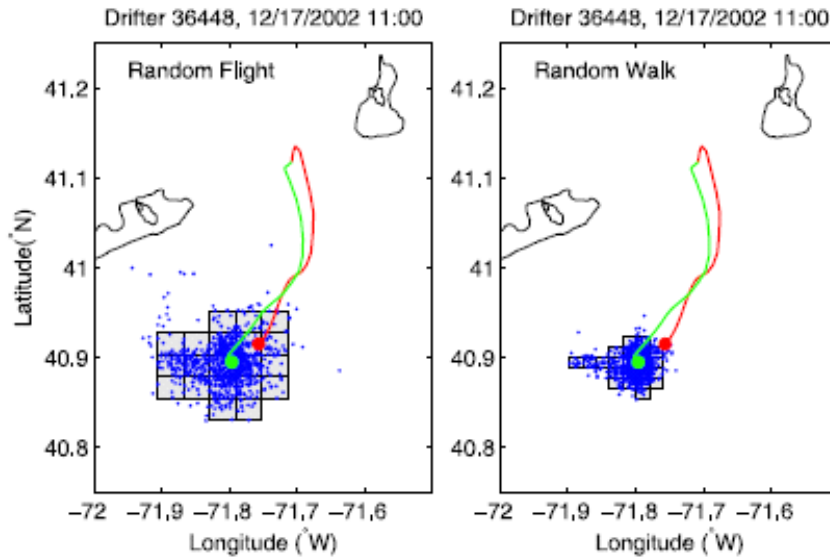


Figure 26. Examples of the precision of random walk versus random flight models from Ullman et al. (2006). Blue dots are end positions of simulated drifter with the boxes delineating the 95th percentile region. Red and green show the trajectories and endpoints of two actual drifters released at the starting location for the modeled drifters. While the random walk model has far less spread in its predictions, it failed to include the actual drifter location shown in red.

VI. Summary of Conclusions:

- Offshore currents (in the region of segment 4) appear to be tidally dominated from what CODAR picks up but it appears to be missing whatever is pulling the real drifter along.
- The random walk and random flight uncertainty models give very similar results in this region.
- GDOP generally adds slightly to uncertainty, except the segment 4 region.
- Our typical 5-hour single-drifter comparisons with a were not long enough to assess uncertainty with much confidence. Longer time periods spanning one or more tidal cycles would produce better comparisons.
- Judrifter with a properly functioning GPS (i.e., set time intervals between fixes) would have helped considerably versus one whose time intervals varied between 11 minutes and 20 hours

Suggestions for improved future research:

- Take 10-12 hour subsets starting at different times within segment 4 in order to compare better with the 10-11 hour segments.
- GPS units on the drifters would enable more frequent model versus measured location comparisons.

VII. APPENDICES

Appendix A: CODAR Antenna Pattern Calibration

The accuracy of surface radial currents derived from individual CODAR stations depends on how well the antenna pattern is known for that particular site. Thus CODAR site calibrations are performed to determine the antenna patterns.

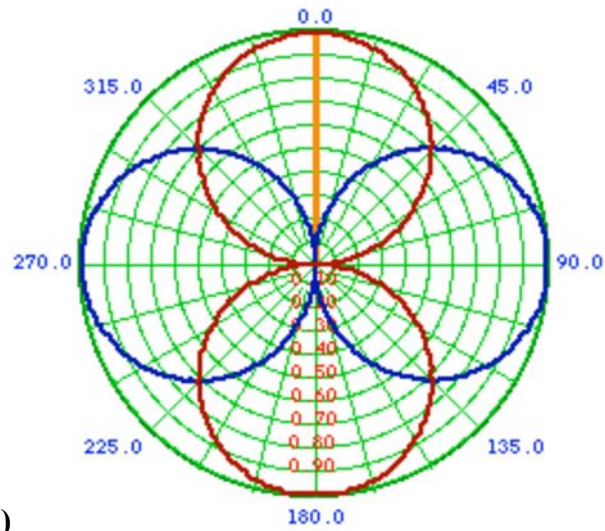
To perform a calibration, the site's transmitter is turned off and is replaced by a portable transponder/antenna that is set to the frequency of the site. The portable transponder sends out a known signal from a known location that is recorded by a hand-held GPS unit. First the proper settings are all stored in their respective units and the portable transponder is been tested to make sure that its signal is being received by the receive antenna. Then the transponder, its antenna, and the GPS unit are taken to the starting position for the calibration track.

The calibration track used is a roughly defined semicircle with its radius centered on the receive antenna. The calibration track can be in the ocean just offshore from the site (a best option) or on the adjacent land/beach seaward of the receive antenna. In the latter case, the local geography the arc may be more or less than 180 degrees. In general, the wider the angle of the arc, the more effective the calibration as the goal is to get the transponder to cover the entire range covered by the station.

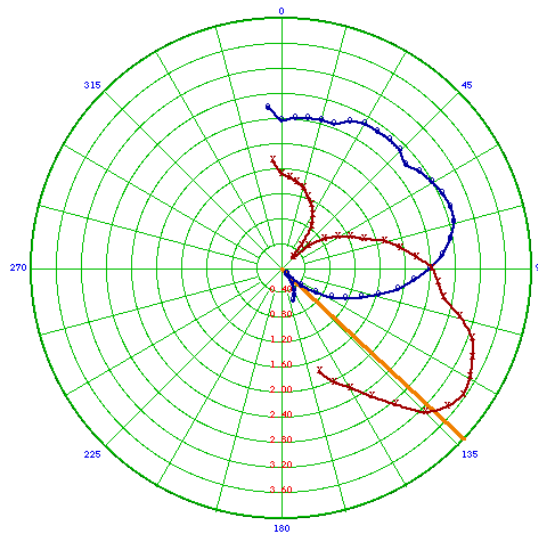
The transponder unit with the GPS is transported back and forth along the calibration track in each direction for at least two full trips. Transport speeds are such that it takes at least half an hour to trace the arc once. In general, more data points are collected with a larger radius of the arc and/or using a slower speed.

The calibration arcs can be done either by walking or by using a boat. A boat is preferred as it can get farther out (one to two kilometers) from the station which allows for a finer resolution and more data points with which to determine the actual antenna pattern of the site. Walking calibrations are very similar but the maximum possible radius is much smaller, resulting in fewer potential data points as well as a possible increase in interference from local sources such as buildings or other antennae. Despite the loss of resolution, walking calibrations can cover a far wider arc, especially in regions where a boat cannot come close enough to the beach to cover the entire spread of the coverage region. Ideally, both walking and boat calibrations are used to get the maximum amount of data over the largest possible area.

The transponder and GPS track data are uploaded into the SeaSonde software which determines the antenna beam pattern of the site by combining the two data sets; compensating for irregularities in the calibration track. Our measured receive antenna beam pattern is shown in Figure A1 relative to an ideal beam pattern.



a)



b)

Figure A1 (a) Ideal antenna beam pattern showing the full 360° pattern (SeaSonde, 2004). (b) Antenna beam pattern from walking calibration on May 29, 2008 at the Nauset CODAR site, courtesy of Hugh from CODAR Ocean Systems. The orange line indicates the bearing of the receive antenna.

Appendix B: Raw and Interpolated Hourly CODAR Maps Corresponding to The Drifter Trajectory Segments

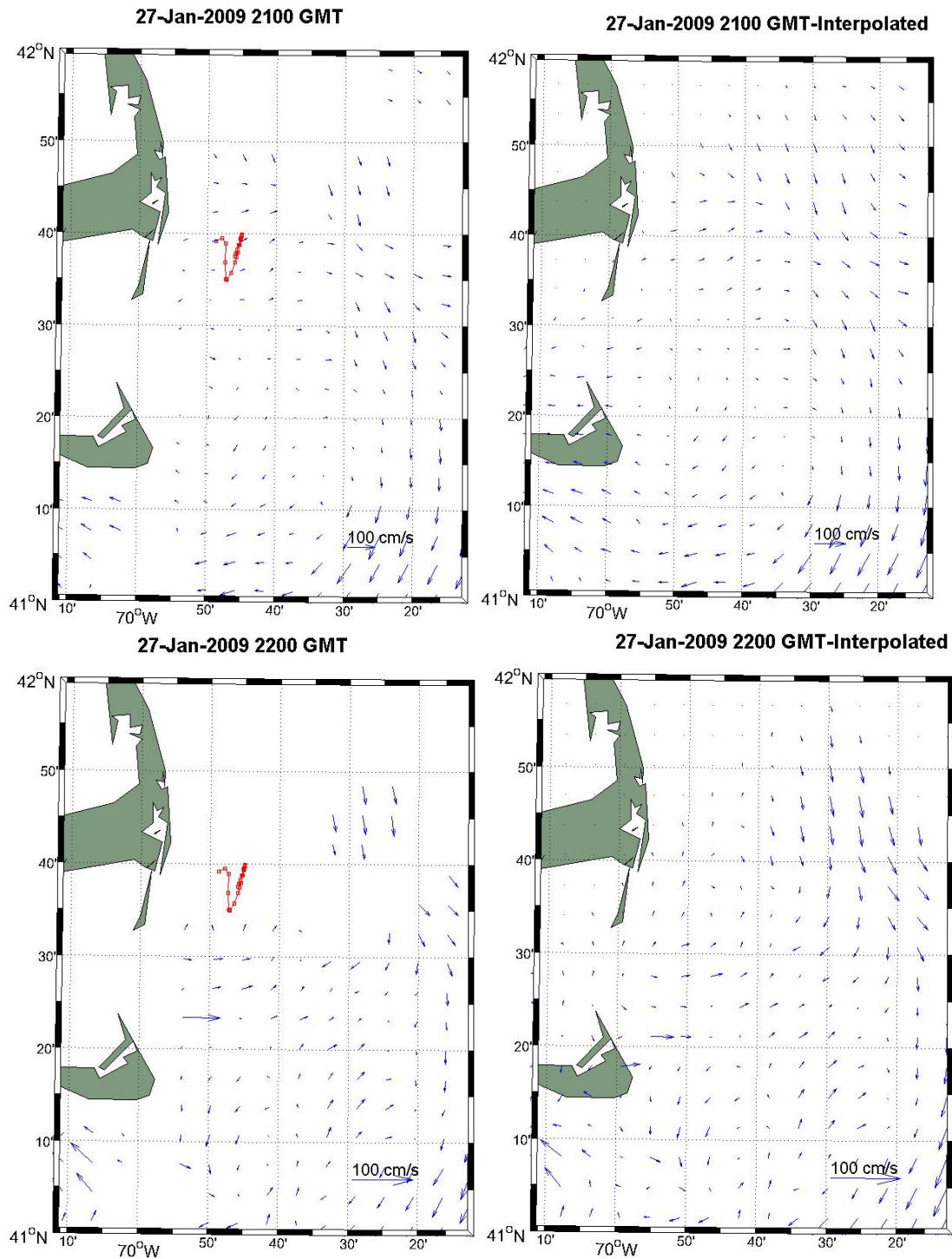


Figure B1 January 27 2009 (left) raw and (right) interpolated CODAR-derived surface current maps for (above) 2100 UTC and (below) 2200 UTC in the Great South Channel- western Gulf of Maine.

Appendix C: Model Drifter Track Segments

Table C1 For segments 1 and 2, the real drifter date/Gregorian times (GMT) /positions/ML => Julian Hour times (hours rel. 0000 UTC 1 Jan 1900)/, and inter-fix elapsed time are given. For the hourly CODAR map JH times (ML), Gregorian times (GMT), and elapsed time from the real drifter deployment.

Date	GMT (hh:mm)	Latitude (deg)	Longitude (deg)	ML date/time (drifter)	dt {t(n+1)- t(n)}	t index (from start)	ML date/time (CODAR)	GMT (hr)
Segment #1 (10 hours)								
28-Jan-09	6:40	41.6149	-69.7667	733801.29				
					1:01	31	733801.29	0700
28-Jan-09	7:41:34	41.5957	-69.7752	733801.32		32	733801.33	0800
					1:27	33	733801.37	0900
28-Jan-09	9:09:09	41.5833	-69.7856	733801.38				
					0:40			
28-Jan-09	9:50:00	41.5836	-69.7888	733801.41		34	733801.41	1000
					2:00	35	733801.45	1100
28-Jan-09	11:50:55	41.6145	-69.7904	733801.49		36	733801.50	1200
					1:56	37	733801.54	1300
28-Jan-09	13:47:16	41.6482	-69.7896	733801.57		38	733801.58	1400
					1:30			
28-Jan-09	15:17:37	41.6586	-69.7976	733801.64		39	733801.62	1500
					1:34	40	733801.66	1600
28-Jan-09	16:51:40	41.6531	-69.8131	733801.70				
Segment #2 (6 hours)								
						85	733803.54	1300
30-Jan-09	13:30:40	41.6265	-69.7312	733803.56		86	733803.58	1400
					1:55	87	733803.63	1500
30-Jan-09	15:26:02	41.6441	-69.7183	733803.64				
					0:25			
30-Jan-09	15:51:42	41.6478	-69.7133	733803.66		88	733803.67	1600
						89	733803.71	1700
					2:25	90	733803.75	1800
30-Jan-09	18:17:10	41.6427	-69.6991	733803.76				

Table C2 For segments 3 and 4, the real drifter date/Gregorian times (GMT) /positions/ML => Julian Hour times (hours rel. 0000 UTC 1 Jan 1900)/, and inter-fix elapsed time are given. For the hourly CODAR map JH times (ML), Gregorian times (GMT), and elapsed time from the real drifter deployment.

Segment #3 (13 hours)

						98	733804.08	0200
31-Jan-09	2:19:35	41.6065	-69.6440	733804.10				
						99	733804.13	0300
					1:41	100	733804.17	0400
31-Jan-09	4:01:16	41.6292	-69.6370	733804.17				
						101	733804.21	0500
					2:20	102	733804.25	0600
31-Jan-09	6:21:17	41.6290	-69.6228	733804.27				
						103	733804.29	0700
					2:08	104	733804.33	0800
31-Jan-09	8:30:02	41.6009	-69.6088	733804.35				
					0:22			
31-Jan-09	8:52:33	41.5905	-69.6052	733804.37				
					0:59		733804.38	0900
31-Jan-09	9:51:39	41.5709	-69.6020	733804.41				
						106	733804.42	1000
						107	733804.46	1100
					2:55	108	733804.50	1200
31-Jan-09	12:46:39	41.5308	-69.5830	733804.53				
						109	733804.54	1300
					1:42	110	733804.58	1400
31-Jan-09	14:29:05	41.4261	-69.4553	733805.60				

Segment #4 (8 hours)

2-Feb-09	23:12:52	41.4778	-69.3471	733806.97				
						168	733807.00	0000
					1:48	169	733807.04	0100
3-Feb-09	1:01:32	41.4451	-69.3347	733807.04				
					0:53			
3-Feb-09	1:54:56	41.4328	-69.3323	733807.08				
					0:11	170	733807.08	0200
3-Feb-09	2:06:05	41.4279	-69.3316	733807.09				
					0:36			
3-Feb-09	2:42:55	41.4214	-69.3320	733807.11				
					0:35		733807.13	0300
3-Feb-09	3:18:10	41.4181	-69.3334	733807.14				
					1:06	172	733807.17	0400
3-Feb-09	4:24:54	41.4193	-69.3383	733807.18				
						173	733807.21	0500
						174	733807.25	0600
					3:32		733807.29	0700
3-Feb-09	7:57:04	41.4565	-69.3644	733807.33				

Table C3 For segment 5, the real drifter date/Gregorian times (GMT) /positions/ML => Julian Hour times (hours rel. 0000 UTC 1 Jan 1900)/, and inter-fix elapsed time are given. For the hourly CODAR map JH times (ML), Gregorian times (GMT), and elapsed time from the real drifter deployment.

Segment #5 (7 hours)

						194	733808.08	0200
4-Feb-09	2:17:04	41.2824	-69.4699	733808.10	1:19			
						195	733808.13	0300
4-Feb-09	3:37:03	41.2638	-69.4971	733808.15	0:47			
						196	733808.17	0400
4-Feb-09	4:25:02	41.2689	-69.5018	733808.18	4:10			
						197	733808.21	0500
						198	733808.25	0600
						199	733808.29	0700
						200	733808.33	0800
4-Feb-09	8:35:35	41.3222	-69.4623	733808.36				

Table C4. For segments 1 and 2, hourly model drifter trajectory positions are given - starting with the time of the real drifter deployment. The inter-hourly average eastward (U) and northward (V) velocity components as well as total speeds are also given.

Hour	Longitude (degrees)	Latitude (degrees)	U velocity (m/hr)	V velocity (m/hr)	Total vel. magnitude (m/hr)
Segment 1					
31	-69.767	41.615	-227.423	534.146	580.545
32	-69.770	41.620	1102.068	-252.996	1130.734
33	-69.756	41.618	-136.444	-657.458	671.467
34	-69.758	41.611	-344.576	102.209	359.416
35	-69.762	41.612	1166.596	-989.268	1529.575
36	-69.748	41.603	-1064.051	361.709	1123.850
37	-69.761	41.607	-2092.211	-112.000	2095.206
38	-69.786	41.606	-705.930	53.700	707.970
39	-69.795	41.606	522.647	-65.729	526.764
40	-69.788	41.606	2.381	-322.379	322.388
Segment 2					
85					
86	-69.731	41.627	300.899	398.550	499.382
87	-69.728	41.630	98.512	543.949	552.797
88	-69.726	41.635	85.592	749.806	754.675
89	-69.725	41.642	283.862	911.332	954.517
90	-69.722	41.650	513.718	648.332	827.188

Table C2: For segments 3, 4 and 5, hourly model drifter trajectory positions are given - starting with the time of the real drifter deployment. The inter-hourly average eastward (U) and northward (V) velocity components as well as total speeds are also given.

Hour	Longitude (degrees)	Latitude (degrees)	U velocity (m/hr)	V velocity (m/hr)	Total vel. magnitude (m/hr)
Segment 3					
98	-69.644	41.607	-463.315	-236.470	520.172
99	-69.650	41.604	-678.745	-411.790	793.892
100	-69.658	41.601	78.067	185.953	201.675
101	-69.657	41.602	655.840	543.920	852.042
102	-69.649	41.607	1998.687	741.898	2131.939
103	-69.625	41.614	1858.886	281.399	1880.065
104	-69.602	41.617	2132.411	-57.227	2133.179
105	-69.576	41.616	2296.277	-163.573	2302.095
106	-69.548	41.615	1937.475	-260.491	1954.908
107	-69.524	41.612	1455.893	-46.293	1456.629
108	-69.507	41.612	733.442	-262.370	778.957
109	-69.498	41.609	0.000	0.000	0.000
Segment 4					
169	-69.335	41.445	401.716	-1892.815	1934.974
170	-69.330	41.428	359.094	-1327.182	1374.904
171	-69.325	41.416	27.887	-531.720	532.451
172	-69.325	41.411	42.353	-194.995	199.542
173	-69.325	41.409	-18.646	249.502	250.198
174	-69.325	41.411	-177.193	900.204	917.478
175	-69.327	41.419	-445.084	956.503	1054.987
Seg. 5					
194	-69.388	41.372	16.117	-1680.259	1680.336
195	-69.388	41.357	406.768	-972.262	1053.923
196	-69.383	41.348	256.605	-917.507	952.714
197	-69.380	41.339	-254.618	-89.855	270.008
198	-69.383	41.339	133.600	972.510	981.644
199	-69.381	41.348	283.009	1144.333	1178.809
200	-69.378	41.358	20.564	933.110	933.337

Appendix D:

Appendix D: Integral Timescale

The timescale T_u needed to calculate the random flight method, according to Ullman et al (2006) and Griffa (1996), is the integral timescale. First a time series of the u/v velocity components were computed for each drifter trajectory segment and then bin-averaged to hourly intervals to compensate for the variable time interval between data points (see Figures D.1-6; Table D2). Second the auto-covariance (Table D.1) was calculated for each of the bin-averaged u and v component time series. The integral timescale (T_u) was calculated according to Davis (1976) using:

$$T_u = \sum_{i=1}^N \rho_{uu}(i\Delta t)\rho_{vv}(i\Delta t) \Delta t \quad , \quad (D.1)$$

where ρ_{uu} and ρ_{vv} are the auto-correlation coefficients, N the number of terms in the time series, and Δt the time interval (one hour).

Table D1. Integral timescales calculated for the u and v components of the velocity for each segment.

Segment 1: $T_{uU} = 2.879$ hrs	$T_{uV} = 2.857$ hrs
Segment 2: $T_{uU} = 2.312$ hrs	$T_{uV} = 2.150$ hrs
Segment 3: $T_{uU} = 2.574$ hrs	$T_{uV} = 3.091$ hrs
Segment 4: $T_{uU} = 3.339$ hrs	$T_{uV} = 3.250$ hrs
Segment 5: $T_{uU} = 2.273$ hrs	$T_{uV} = 2.001$ hrs

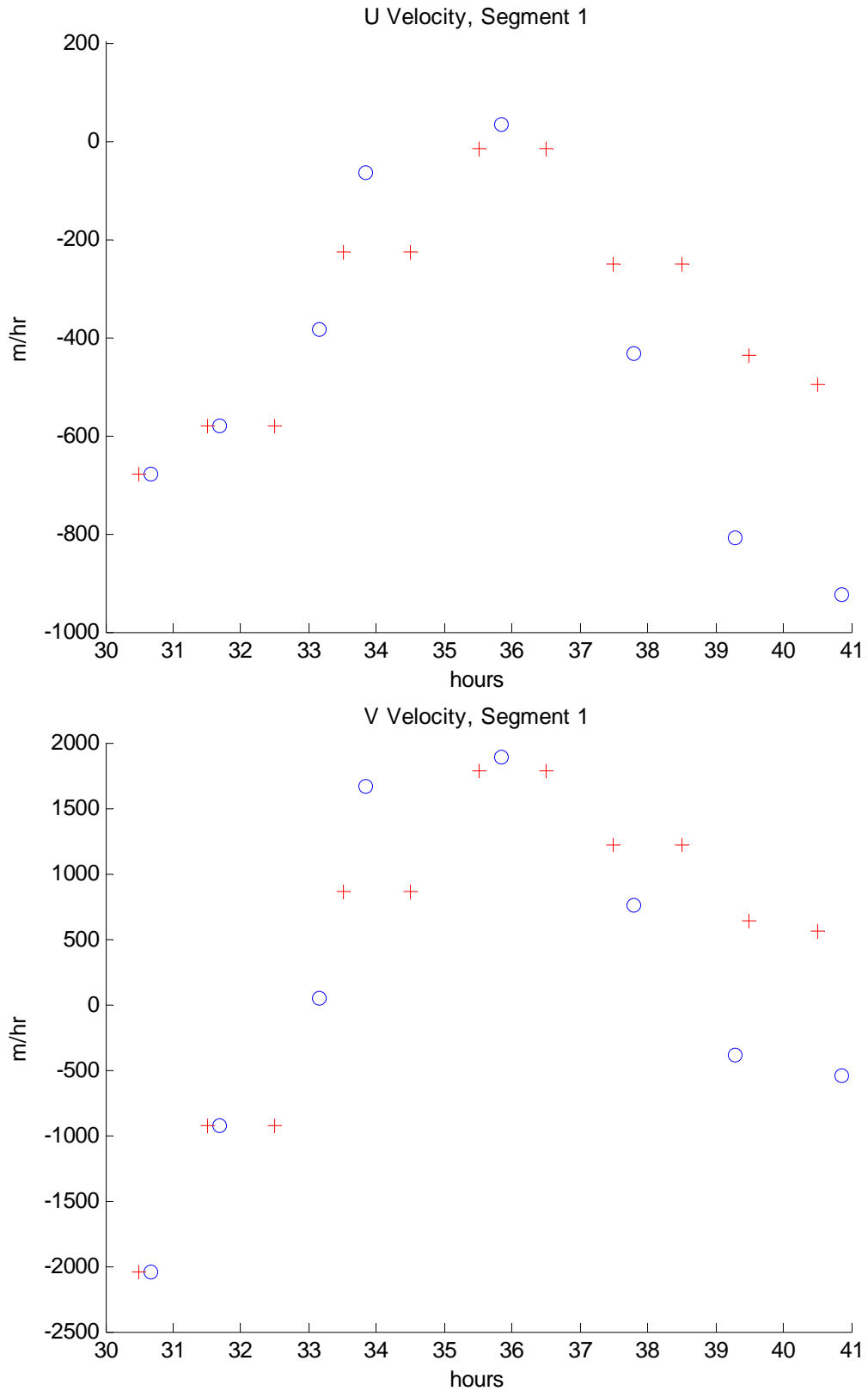


Figure D1. Segment 1 time series of drifter u (top) and v (bottom) velocity components for both the raw (circles) and bin averaged (crosses) values.

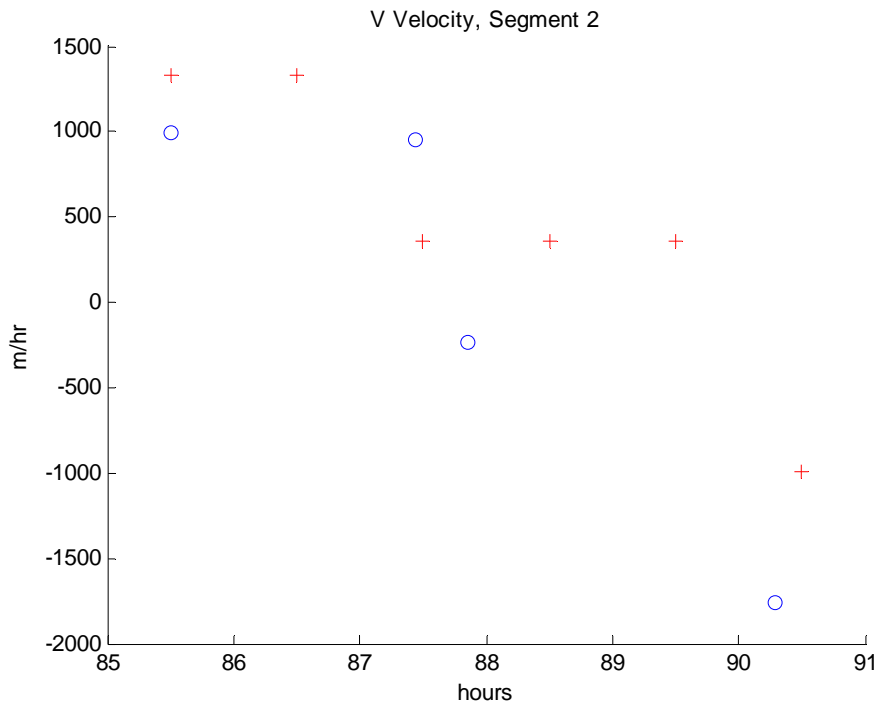
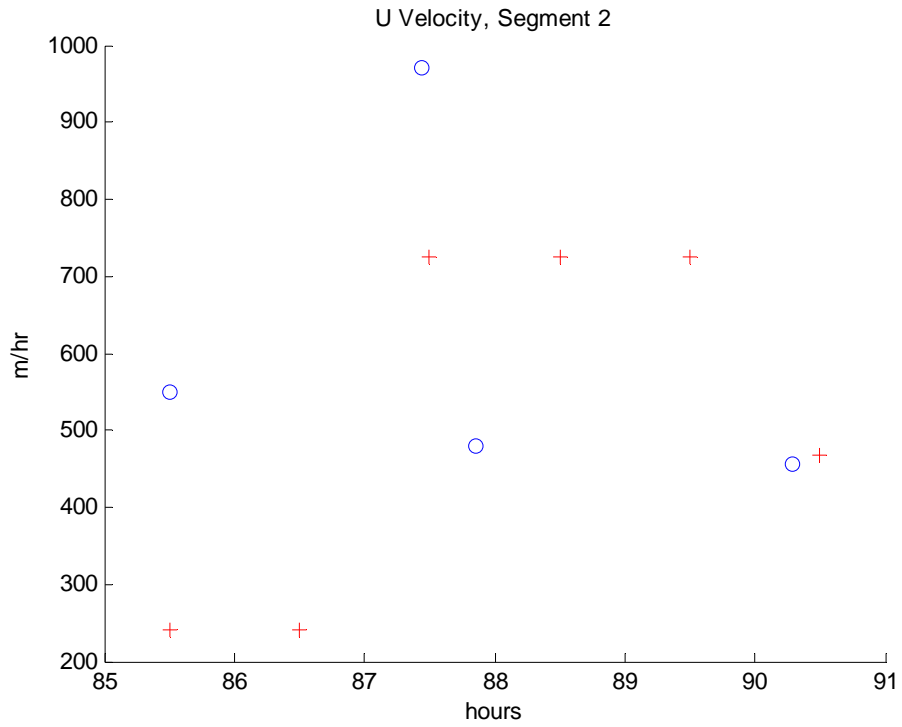


Figure D2. Segment 2 time series of drifter u (top) and v (bottom) velocity components for both the raw (circles) and bin averaged (crosses) values.

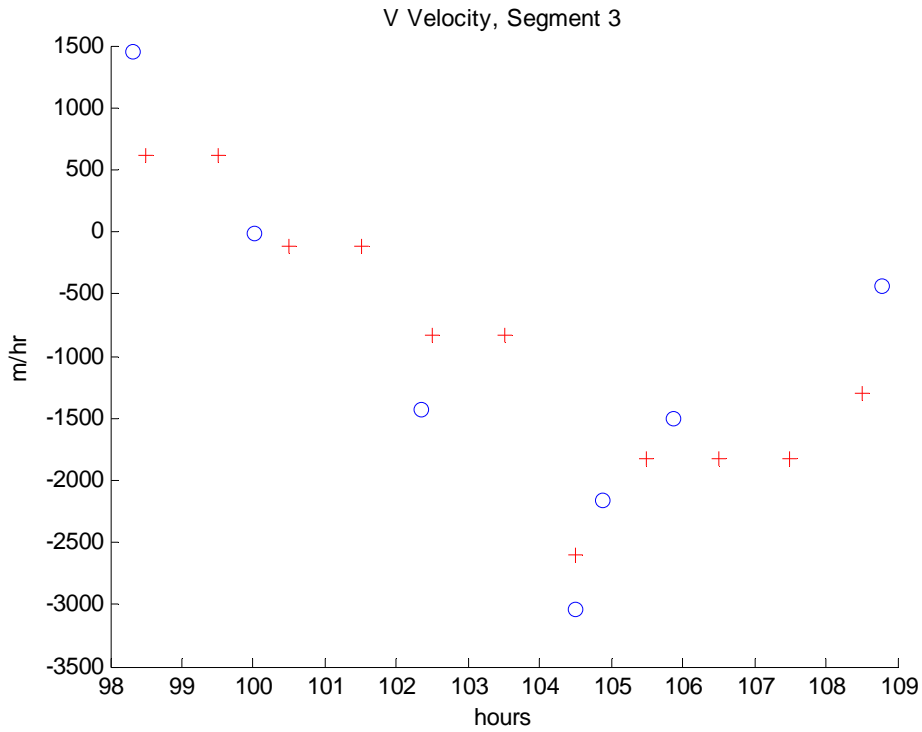
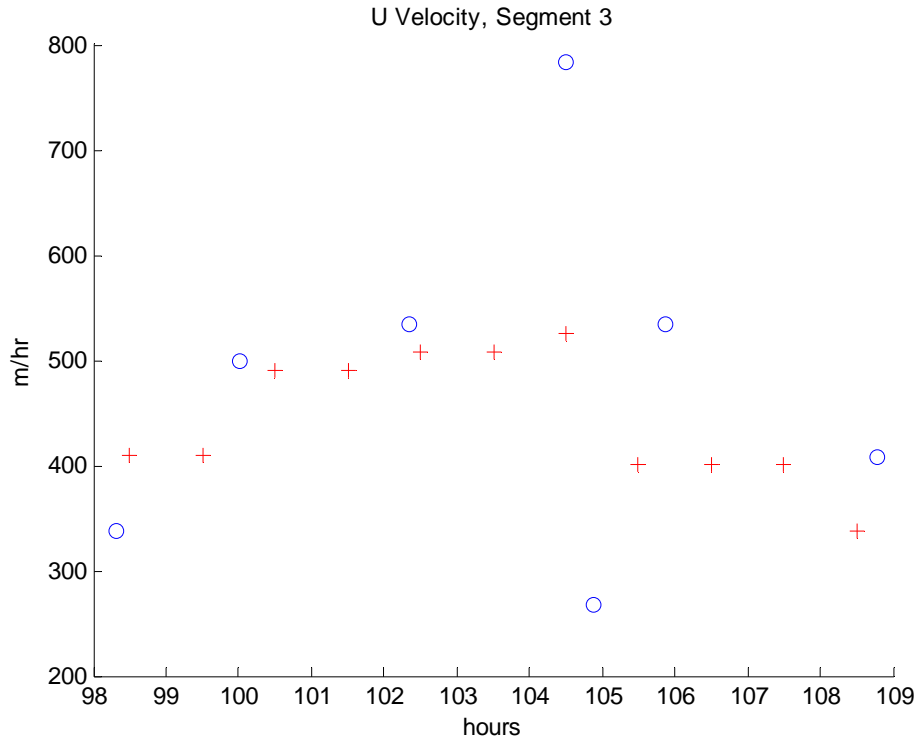


Figure D3. Segment 3 time series of drifter u (top) and v (bottom) velocity components for both the raw (circles) and bin averaged (crosses) values.

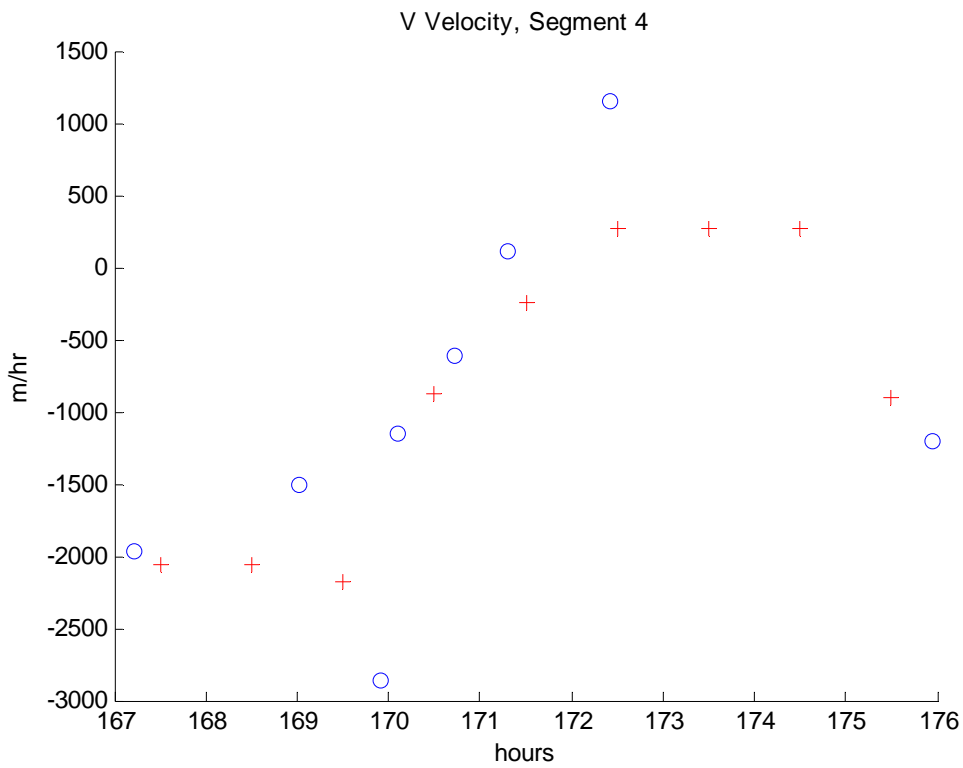
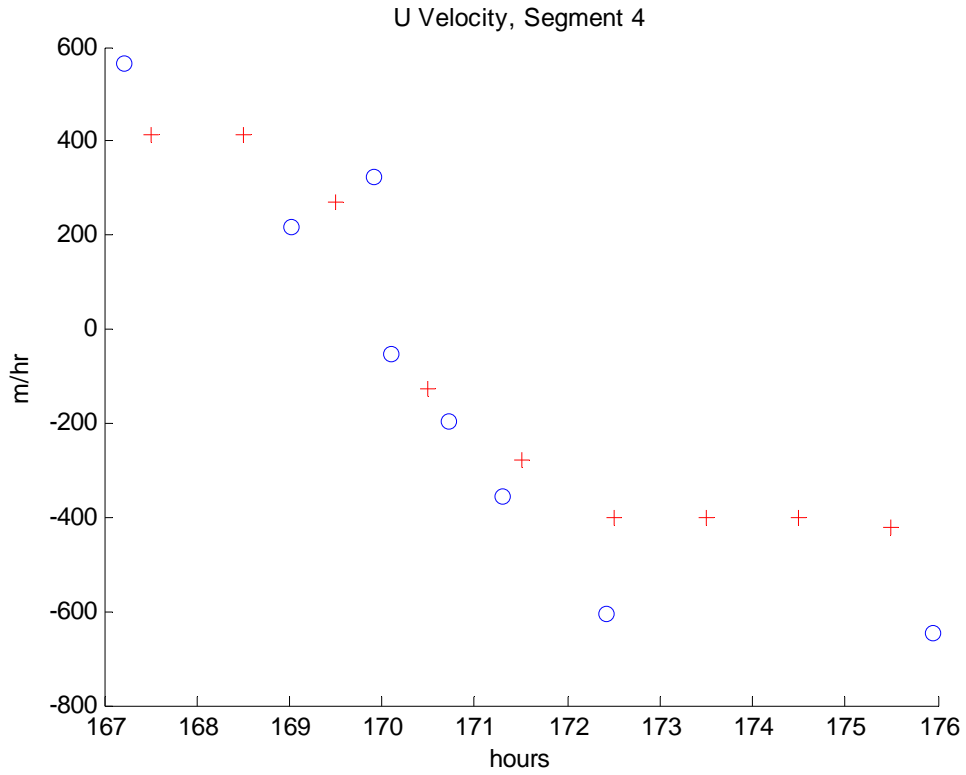


Figure D4. Segment 4 time series of drifter u (top) and v (bottom) velocity components for both the raw (circles) and bin averaged (crosses) values.

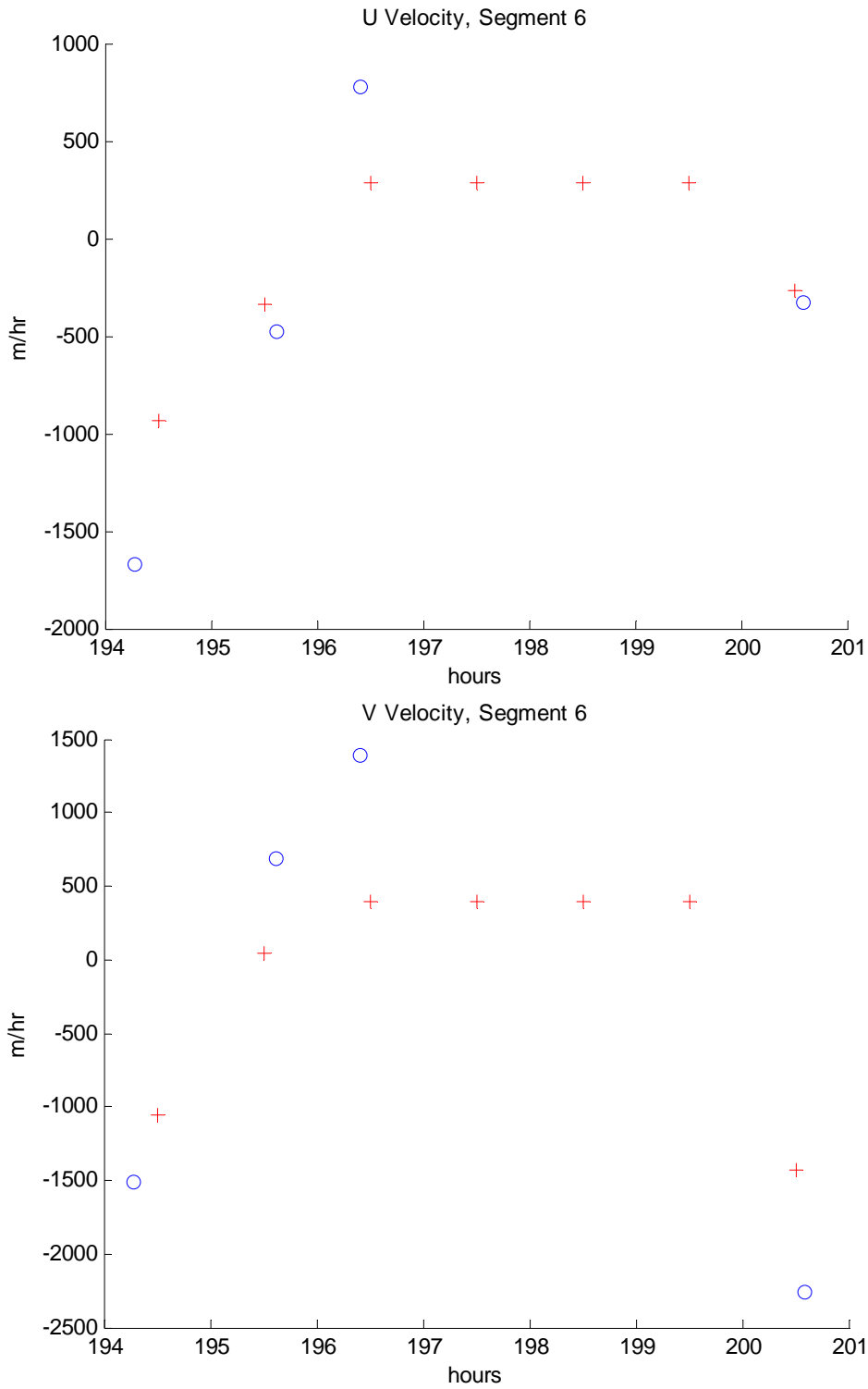


Figure D5. Segment 5 time series of drifter u (top) and v (bottom) velocity components for both the raw (circles) and bin averaged (crosses) values.

Table D2. Bin average series used to calculate the integral timescales.

Segment 1			Segment 2			Segment 3		
u (m/hr)	v (m/hr)	t (hr)	u (m/hr)	v (m/hr)	t (hr)	u (m/hr)	v (m/hr)	t (hr)
-680.682	-2050.74	30.5	241.367	1332.382	85.5	409.098	611.0542	98.5
-580.97	-924.002	31.5	241.367	1332.382	86.5	409.098	611.0542	99.5
-580.97	-924.002	32.5	725.208	362.0614	87.5	489.786	-119.444	100.5
-225.746	857.476	33.5	725.208	362.0614	88.5	489.786	-119.444	101.5
-225.746	857.476	34.5	725.208	362.0614	89.5	507.17	-829.746	102.5
-16.4	1782.05	35.5	467.605	-993.631	90.5	507.17	-829.746	103.5
-16.4	1782.05	36.5				525.497	-2598.61	104.5
-249.936	1213.92	37.5				401.185	-1830.56	105.5
-249.936	1213.92	38.5				401.185	-1830.56	106.5
-438.413	643.928	39.5				401.185	-1830.56	107.5
-494.952	560.986	40.5				337.553	-1302.24	108.5

Segment 4			Segment 5		
u (m/hr)	v (m/hr)	t (hr)	u (m/hr)	v (m/hr)	t (hr)
415.699	-2063.25	168	-935.62	-1059.58	194.5
415.699	-2063.25	169	-337.55	41.55173	195.5
269.78	-2180.9	170	288.23	391.3397	196.5
-124.64	-880.282	171	288.23	391.3397	197.5
-277.57	-247.141	172	288.23	391.3397	198.5
-401.595	270.433	173	288.23	391.3397	199.5
-401.595	270.433	174	-263.3	-1431.79	200.5
-401.595	270.433	175			
-422.874	-903.3	176			

Appendix E: Model Drifter Trajectories

Observed drifter trajectory segments (blue) are compared in Figures E1-E3 with average (black dots) of an ensemble of model drifter trajectories (green with red endpoints). Ensembles of model trajectories were derived using (left) random walk and (right) random flight uncertainty models, respectively.

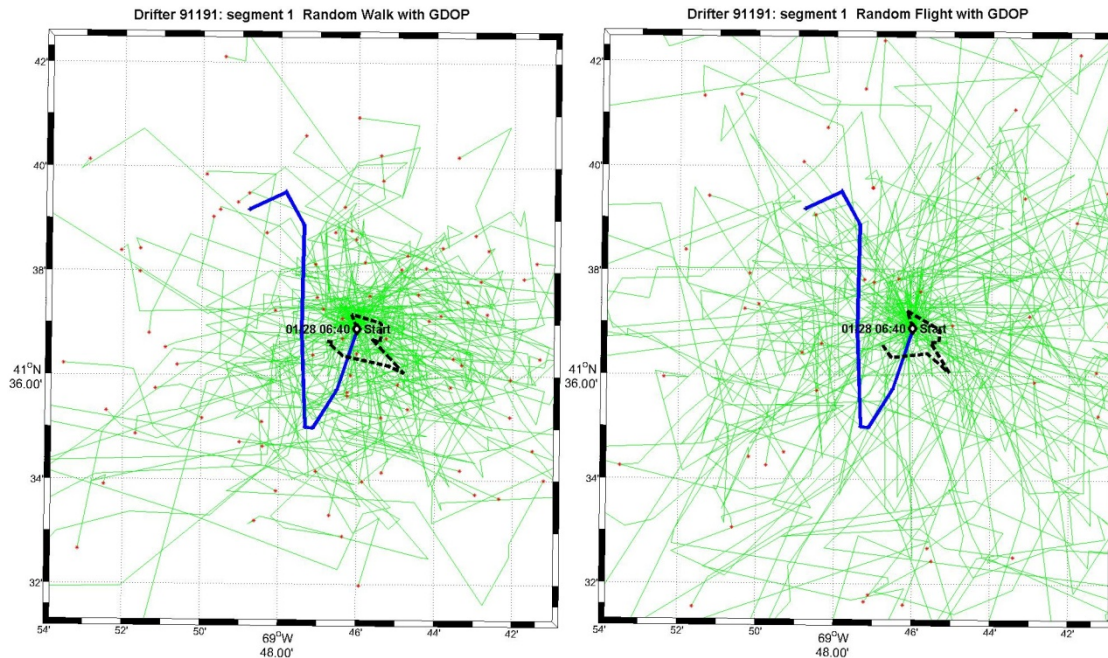


Figure E1 Observed drifter trajectory *segment 1* (blue) is compared with average model drifter trajectories derived using (left) random walk and (right) random flight uncertainty models, respectively.

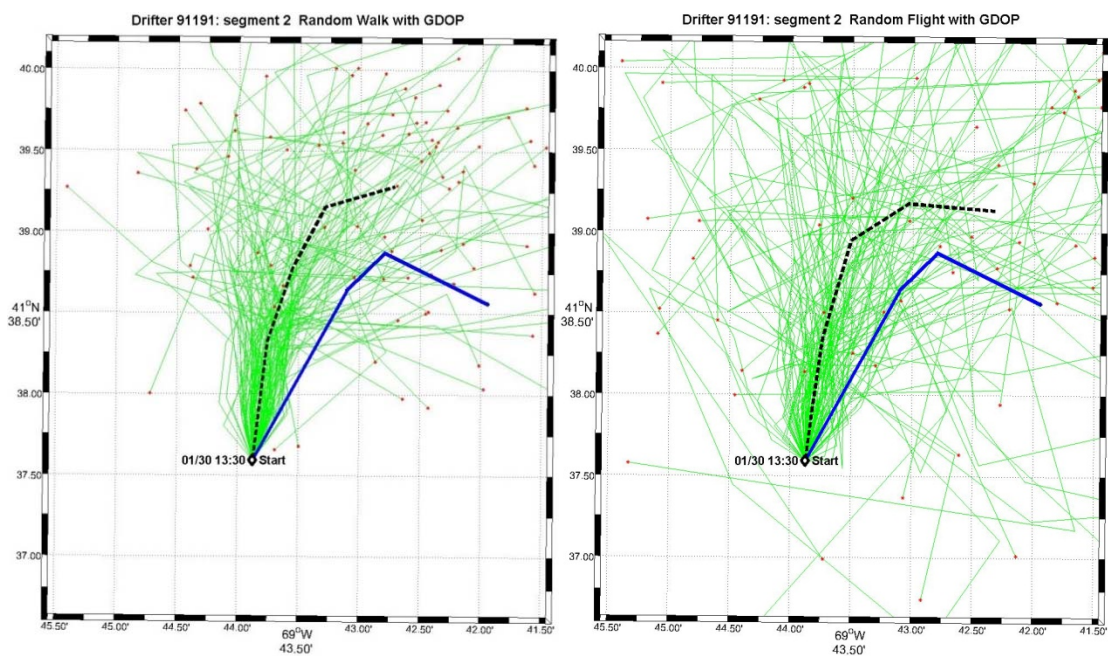


Figure E2 Observed drifter trajectory *segment 2* (blue) is compared with average model drifter trajectories derived using (left) random walk and (right) random flight uncertainty models, respectively.

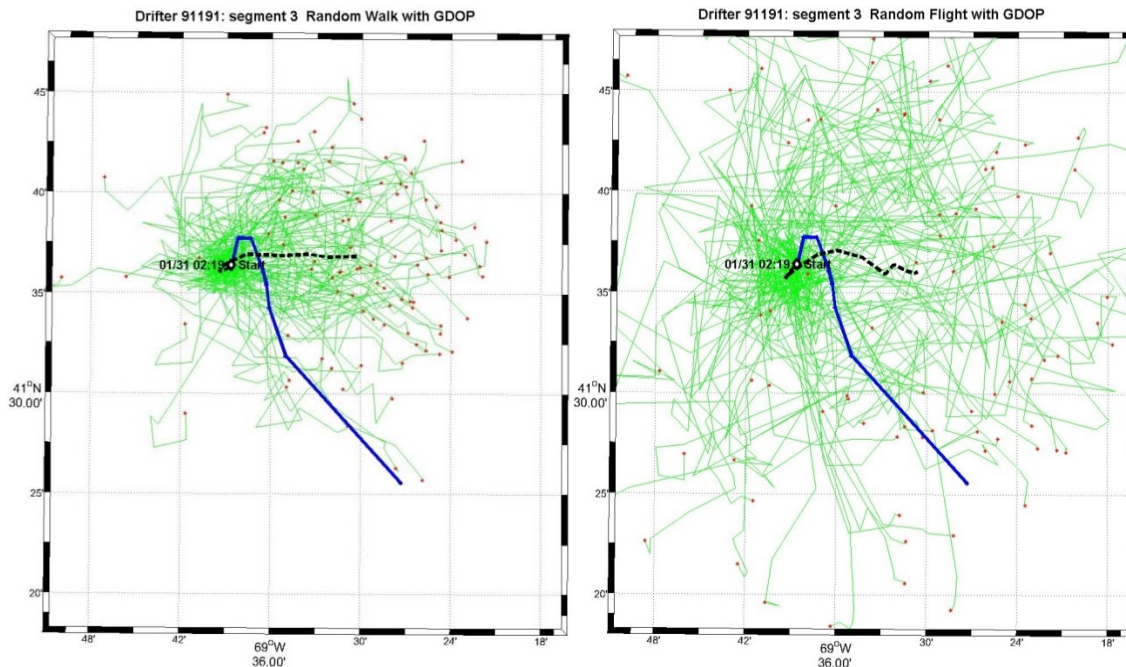


Figure E3 Observed drifter trajectory *segment 3* (blue) is compared with average model drifter trajectories derived using (left) random walk and (right) random flight uncertainty models, respectively.

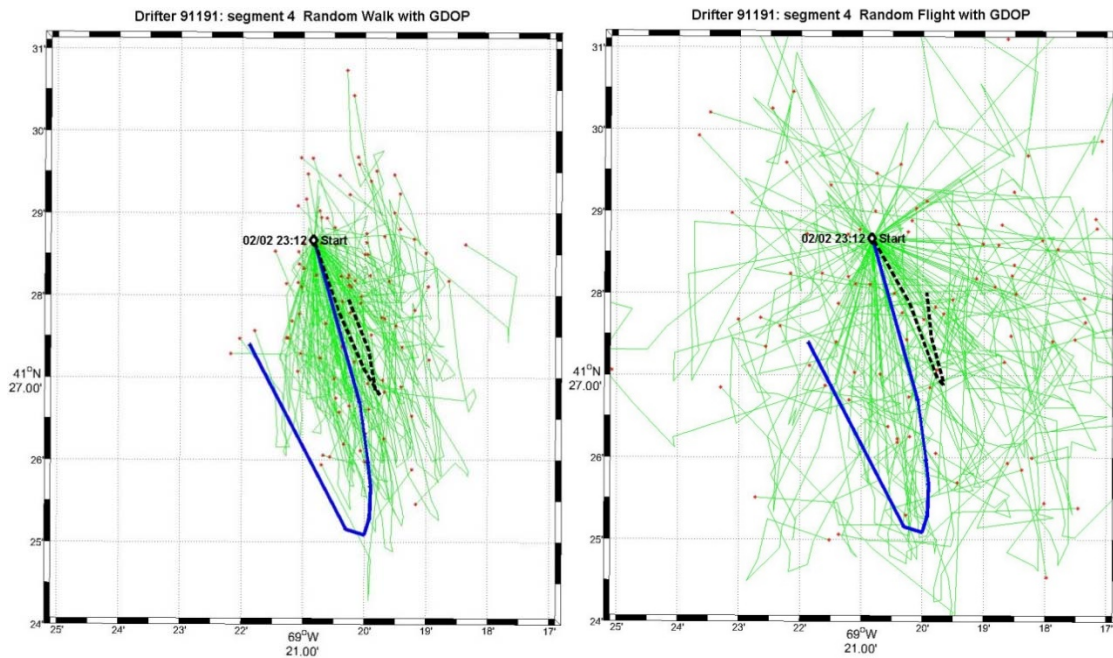


Figure E4 Observed drifter trajectory *segment 4* (blue) is compared with average model drifter trajectories derived using (left) random walk and (right) random flight uncertainty models, respectively.

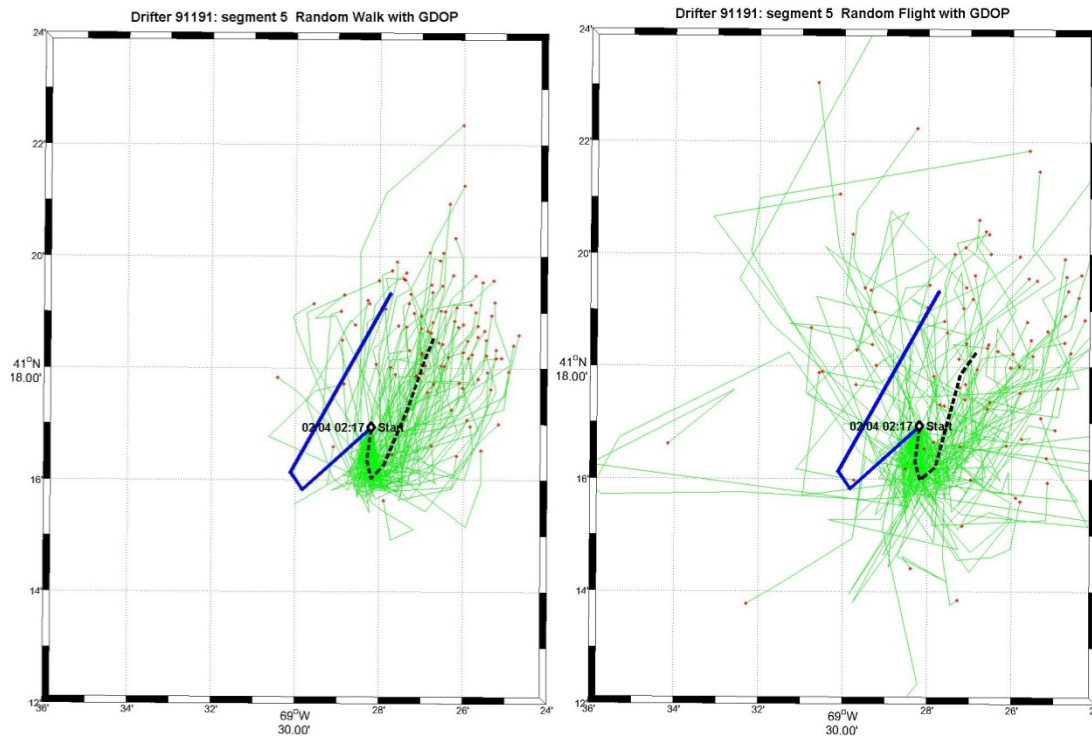


Figure E5 Observed drifter trajectory *segment 5* (blue) is compared with average model drifter trajectories derived using (left) random walk and (right) random flight uncertainty models, respectively.

VIII. ACKNOWLEDGMENTS

This study was conducted within the context of a MIT Sea Grant-funded project entitled “An Investigation of Transient Tidal Eddies in the Western Gulf of Maine” (see <http://www.smast.umassd.edu/OCEANOL/tte.php>).

IX. REFERENCES

- Barrick, D. E. (1972), First-order theory and analysis of mf/hf/vhf scatter from the sea, *IEEE Trans. Antennas Propag.*, AP-20, 2-10.
- Barrick, D.E., (2005). "Effects of Shallow Water on Radar Measurements", CODAR report, January.
- [SKL: <http://www.codar.com/Manuals/SeaSonde/Docs/Informative/Total_Velocity_Uncertainties.pdf> CODAR documentation (the only one actually including the standard deviation formulas) but no author/date given for this particular portion
- Barrick, D. E. (1972), First-order theory and analysis of mf/hf/vhf scatter from the sea, *IEEE Trans. Antennas Propag.*, AP-20, 2-10.
- Battisti, D. S., and A. J. Clarke (1982), A simple method for estimating barotropic tidal currents on the continental margins with specific application to the M2 tide off the Atlantic and Pacific coasts of the United States, *J. Phys. Oceanogr.*, 12, 8-16.
- Barrick, D. E. (2006). Geometrical dilution of statistical accuracy (GDOSA) in Multi-Static HF radar networks, CODAR report, revised 24 January 2006.
- Brown, W. S. (1984). A Comparison of Georges Bank, Gulf of Maine, and New England Shelf Tidal dynamics, *J. Phys. Oceanogr.* 14, 145-167.

- Brown, W.S. and J.D. Irish, 1993. The annual variation of water mass structure in the Gulf of Maine, *Journal of Marine Research*, 51, 53-107.
- Brown, W.S., Z. Yu, J. Kohut, and S. Glenn, 2007. Transient tidal eddies in the western Gulf of Maine; *to be submitted JGR*.
- Brown, W. S. and Z. Yu (2006). CODAR measurement and model simulation of transient tidal eddies in the western Gulf of Maine, *SMAST Technical Report 06-0503*.
http://www.smast.umassd.edu/OCEA_NOL/reports.php
- Brown, W.S., G. M. Marques, S. King, C. Jakubiak, D. Brown, E. Levine, & L. Goodman, (2009). Transient Tidal Eddy Project Data Report: Winter 2008-09, SMAST Technical Report 09-0204 http://www.smast.umassd.edu/OCEANOL/reports/TTE/WINTER_08-09_DataRPT_13may09.pdf
- Chapman, R. D., L. K. Shay, H. C. Graber, J. B. Edson, A. Karachintsev, C. L. Trump, and D. B. Ross (1997), On the accuracy of HF radar surface current measurements: Intercomparisons with ship-based sensors, *J. Geophys. Res.*, 102, 18,737-18,748.
- Crombie, D. D. (1955), Doppler spectrum of sea echo at 13.56 Mc/s, *Nature*, 175, 681-682.
- Davis, R.E. (1976), Predictability of sea surface temperature and sea level pressure anomalies in the north Pacific, *J. Phys. Oceanogr.*, 6, 249-266.
- Emery, B. M., L. Washburn, and J. A. Harlan (2004). Evaluating Radial Current Measurements from CODAR High-Frequency Radars with Moored Current Meters, *J. Atmos. Ocean Tech.*, 1259-1271.
- Essen, H. H., K. W. Gurgel, and T. Schlick (2000). On the Accuracy of Current Measurements by Means of HF Radar, *IEEE J. of Oceanic Eng.*, 25(4), 472-480.
- Geyer, W. R. (1993). Three-dimensional flow around headlands, *J. Geophys. Res.*, 98, 955-966.
- Geyer, W. R., and R. Signell (1990). Measurements of tidal flow around a headland with a shipboard acoustic Doppler current profiler, *J. Geophys. Res.*, 95, 3189-3197.
- Griffa, A., K. Owens, L. Piterbarg, and B. Rozovskii (1995). Estimates of turbulence parameters from Lagrangian data using a stochastic particle model, *J. Mar. Res.*, 53, 371-401.
- Holboke, Monica J., 1998. "Variability of the Maine Coastal Current under Spring Conditions", Ph.D. Dissertation -Thayer School of Engineering -Dartmouth College, pp. 193.
- Kohut, J., and S. M. Glenn, (2003), "Improving HF radar surface current measurements using measured antenna beam patterns", *J. Atmos. Ocean Tech.*, 1303–1316.
- Lipa, B. (2003). Uncertainties in Seasonal Current Velocities, *Proc. of the IEEE/OES Seventh working Conference on Current Measurement Technology*.
- Lipa, B. J., and D. E. Barrick (1983). Least-Squares Methods for the Extraction of Surface Currents from CODAR Crossed-Loop Data: Application at ARSLOE, *IEEE J. of Oceanic Eng.*, OE-8(4).
- Lynch, D. R. and C. E. Naimie (1993). The M₂ Tide and Its Residual on the Outer Banks of the Gulf of Maine, *J. Phys. Oceanogr.* 23, 2222-2253.
- Lynch, D.R., J.T.C. Ip, C.E. Naimie, and F.E. Werner, 1996. Comprehensive coastal circulation model with application to the Gulf of Maine. *Continental Shelf Research*, 16, 875-906.
- Lynch, D. R., M. J. Holboke, and C.E. Naimie, 1997. The Maine coastal current: spring climatological circulation. *Continental Shelf Research*, 17, 605-634.
- Manning, J.P., et al., 2009. Drifter observations of the Gulf of Maine Coastal Current, *Continental Shelf Research*, doi:10.1016/j.csr.2008.12.008
- Moody, J., B. Butman, R.C. Beardsley, W.S. Brown, W. Boicourt, P. Daifuku, J.D. Irish, D.A. Mayer, H.E. Mofjeld, B. Petrie, S. Ramp, D. Smith and W.R. Wright, 1984."Atlas of Tidal Elevation and Current Observations on the Northeast American Continental Shelf

- and Slope," *U.S. Geological Survey Bulletin No. 1611*, U.S. Government Printing Office, pp. 122.
- Nishimoto, and M.M., Washburn, L. (2002). "Patterns of coastal eddy circulation and abundance of pelagic juvenile fish in the Santa Barbara Channel, California, USA", *Marine Ecological Progress Series*, 241, 183-199.
- NOAA, (2009). "NOAA, U.S. Coast Guard: New Ocean Current Data to Improve Search and Rescue Activities." NOAA press release, May 4, 2009.
http://www.noaanews.noaa.gov/stories2009/20090504_ious.html
- NOAA Center for Operational Oceanographic Products and Services (CO-OPS).
<http://tidesandcurrents.noaa.gov/>
- O'Donnell, J., D. Ullman, M. Spaulding, E. Howlett, T. Fake, P. Hall, T. Isaji, C. Edwards, E. Anderson, T. McClay, J. Kohut, A. Allen, S. Lester, C. Turner, and M. Lewandowski (2005). Integration of Coastal Ocean Dynamics Application Radar (CODAR) and Short-Term Predictive System (STPS) Surface Current Estimates into the Search and Rescue Optimal Planning System (SAROPS), *U. S. Coast Guard Rep., CG-D-01-2006*.
- Pingree, R., and L. Maddock, 1980. The effects of bottom friction and Earth's rotation on an island's wake. *J. Mar. Biol. Assoc. U.K.*, 60, 499-508.
- Schaefer, R (2003). Search and Rescue Summary Statistics with Performance Measures Fiscal Years 1994-2003, USCG Office of Search and Rescue, 11/13/03.
<http://152.121.2.2/hq/g-o/g-opr/94-03summary.doc>
- SeaSonde Radial Application Guide for CrossLoopPatterner, Codar Ocean Sensors, July 20, 2004. http://www.codar.com/Manuals/SeaSonde/Docs/GuidesToTheApplications/Guide_CrossLoopPatterner.pdf
- Shearman, R. K. and S. J. Lentz (2004). Observations of tidal variability on the New England shelf, *J. Geophys. Res.*, 109, C06010, doi: 10.1029/2003/JC001972.
- Signell, R. P. and W. R. Geyer, 1991. Transient Eddy Formation Around Headlands, *J. Geophys. Res.*, 96(C2), 2561-2575.
- Stewart, R. H., and J. W. Joy (1974), HF radio measurement of surface currents, *Deep Sea Res.*, 21, 1039-1049.
- Stokesbury, K., 2002. Cooperative Fisheries Science Forum I: Scallops May 2-3, 2002, *SMAST Tech. Rpt. No. SMAST-05-03-01*.
- Thompson, K. R., J. Sheng, P. C. Smith, and L. Cong (2004). Prediction of surface currents and drifter trajectories on the inner Scotian Shelf, *J. Geophys. Res.*, 108(C9), 3287, doi: 10.1029/2001JC001119.
- Tremblay, M. J., J. W. Loder, F. E. Werner, C. E. Naimie, F. H. Page, M. M. Sinclair, 1994. Drift of sea scallop larvae *Placopecten magellanicus* on Georges Bank: a model study of the roles of mean advection, larval behavior, and larval origin, *Deep Sea Research II*, 41(1), 7-49.
- Ullman, D. S., J. O'Donnell, J. Kohut, T. Fake, and A. Allen (2006). Trajectory prediction using HF radar surface currents: Monte Carlo simulation of prediction uncertainties, *J. Geophys. Res.*, 111, C12005, doi: 10.1029/2006JC003715.
- Ullman, D. S., J. O'Donnell, C. Edwards, T. Fake, D. Morschauser, M. Sprague, A. Allen, and B. Krenzien (2003). Use of Coastal Ocean Dynamics Application Radar (CODAR) technology in U. S. Coast Guard search and rescue planning, *U. S. Coast Guard Rep., CG-D-09-03*.

